International Journal of Biological Macromolecules 280 (2024) 135703

Contents lists available at ScienceDirect

International Journal of Biological Macromolecules

journal homepage: www.elsevier.com/locate/ijbiomac

Injectable mineralized Sr-hydroxyapatite nanoparticles-loaded ε-polylysine-hyaluronic acid composite hydrogels for bone regeneration

A. Rubina [a,b], A. Sceglovs [a,b], A. Ramata-Stunda [c], I. Pugajeva [d], I. Skadins [e], A.R. Boyd [f], A. Tumilovica [a,b], L. Stipniece [a,b,*], K. Salma-Ancane [a,b,*]

[a] Institute of Biomaterials and Bioengineering, Faculty of Natural Sciences and Technology, Riga Technical University, Pulka St. 3/3, Riga LV-1007, Latvia
[b] Baltic Biomaterials Centre of Excellence, Headquarters at Riga Technical University, Riga, Latvia
[c] Department of Microbiology and Biotechnology, Faculty of Biology, University of Latvia, Jelgavas St. 1, Riga LV-1004, Latvia
[d] Institute of Food Safety, Animal Health and Environment "BIOR", Lejupes Street 3, Riga LV-1076, Latvia
[e] Department of Biology and Microbiology, Riga Stradins University, Dzirciema St. 16, Riga LV-1007, Latvia
[f] Nanotechnology and Integrated Bioengineering Centre (NIBEC), School of Engineering, Ulster University, Shore Road, Newtownabbey, Co. Antrim, BT37 0QB, United Kingdom of Great Britain and Northern Ireland

ARTICLE INFO

Keywords:
Sr-substituted hydroxyapatite nanoparticles
Injectable nanocomposite hydrogels
Sr ion delivery
Antibacterial hydrogels
Osteogenic potential

ABSTRACT

In this study, multifunctional injectable mineralized antibacterial nanocomposite hydrogels were prepared by a homogenous distribution of high content of (up to 60 wt%) Sr-substituted hydroxyapatite (Sr-HAp) nanoparticles into covalently cross-linked ε-polylysine (ε-PL) and hyaluronic acid (HA) hydrogel network. The developed bone-targeted nanocomposite hydrogels were to synergistically combine the functional properties of bioactive Sr-HAp nanoparticles and antibacterial ε-PL-HA hydrogels for bone tissue regeneration. Viscoelasticity, injectability, structural parameters, degradation, antibacterial activity, and *in vitro* biocompatibility of the fabricated nanocomposite hydrogels were characterized. Physical performances of the ε-PL-HA hydrogels can be tailored by altering the mass ratio of Sr-HAp. The nanocomposite hydrogels revealed good stability against enzymatic degradation, which increased from 5 to 19 weeks with increasing the mass ratio of Sr-HAp from 40 % to 60 %. The loading of the Sr-HAp at relatively high mass ratios did not suppress the fast-acting and long-term antibacterial activity of the ε-PL-HA hydrogels against *S. aureus* and *E. coli*. The cell studies confirmed the cytocompatibility and pre-collagen I synthesis-promoting activity of the fabricated nanocomposite hydrogels.

1. Introduction

Bone defects and fracture regeneration remain a major medical challenge in modern clinical practice [1]. One of the main reasons is the global silent epidemic - osteoporosis. According to the World Health Organization (WHO), metabolic bone disease - osteoporosis, is the second most prevalent illness globally, after cardiovascular diseases [2]. Osteoporosis can cause complex fragility fractures and critical-size bone defects (defects involving 50 % of the cortical diameter with a minimum length of 1 cm [3]), which need complex surgical intervention and reconstruction. The costs of healthcare systems attributed to osteoporotic fractures in the European Union are around €37 billion per year, predicted to double by 2050 [4]. Thus, there is an urgent need for multifunctional bone-targeted biomaterials with promising therapeutic and regeneration capabilities [5].

The current treatment protocols for complex osteoporotic fractures involve the use of auto/allografts [6], inert metallic implants [7], or bioactive ceramic implants [8], but their use is associated with various limitations. The gold standard, autografts, are expensive and of low availability, while allografts also have limited availability and possess infection risks [9]. Inert metallic implants offer high mechanical strength but lack bioactivity and bioresorbability and cannot fully integrate with bone tissues. In turn, bioactive calcium phosphate (CaP) bone biomaterials demonstrate excellent biocompatibility and bioactivity in physiological conditions due to their similarity with the major inorganic component of bone tissue and can form intimate functional interfaces with bone tissue. However, CaP biomaterials have low mechanical strength, uncertain degradation rate, lack of cohesiveness, and

* Corresponding authors at: Institute of Biomaterials and Bioengineering, Faculty of Natural Sciences and Technology, Riga Technical University, Pulka St. 3/3, Riga LV-1007, Latvia.
E-mail addresses: liga.stipniece@rtu.lv (L. Stipniece), kristine.salma-ancane@rtu.lv (K. Salma-Ancane).

https://doi.org/10.1016/j.ijbiomac.2024.135703
Received 9 April 2024; Received in revised form 11 September 2024; Accepted 14 September 2024
Available online 16 September 2024

mechanical integrity [9,10]. Moreover, the commercially available bone biomaterials have limited regeneration potential for bone-related disease treatment and are still far from those of the unique composite structure of bone.

Bone is a complex inorganic-organic nanocomposite composed of extracellular matrix (ECM) and several types of cells [11]. The bone ECM consists of 20–40 % organic matrix, 50–70 % minerals, mostly hydroxyapatite (HAp) nanocrystallites between and within the length of collagen fibers, and 5–10 % water. The organic matrix is composed of type I collagen (90 %) and over 200 different non-collagenous proteins (~10 %), of which proteoglycans and glycosaminoglycans, including non-sulfated glycosaminoglycan hyaluronic acid (HA), play a significant role in physiological bone remodeling [12,13].

Injectable natural biopolymer-based hydrogels have been extensively explored as versatile biomaterials for bone tissue engineering applications due to their advantageous functionalities such as biocompatibility and non-toxicity, ability to mimic three-dimensional (3D) ECM, intrinsic cellular interactions, rheological properties, and biodegradability [14,15]. Moreover, the main advantages of the injectable hydrogels as bone-targeted biomaterials include the ability to mimic the bone ECM, provide a functionalized microenvironment for bone defect regeneration, form the desired shape to fill internal large and irregular defects, locally administrate drugs or biologically active molecules directly to the bone defect site over a long period, improve therapeutic efficiency, and decrease toxic effects [16–19]. Among the variety of naturally derived biopolymers, hyaluronic acid (HA) is one of the most versatile biopolymers for bone regeneration, providing an extracellular environment for osteogenesis-related cells and initiating many cellular signaling pathways in bone regeneration [20,21]. Extensively researched injectable HA-based hydrogels have shown their superior potential to mimic the natural extracellular matrix of bone tissue and provide a suitable microenvironment for cell support and tissue regeneration [22], such as osteogenesis, tunable rheological/mechanical properties, biocompatibility, biodegradability, and mass transferability [23]. Recently, ε-poly-L-lysine (ε-PL) as an antimicrobial polypeptide has been extensively researched as a high-performance component for developing antibacterial biomaterials due to its antifungal and antibacterial properties, solubility, biodegradability, and non-toxicity to humans and the environment [24]. In our earlier studies, ε-PL was used to achieve an inherent antibacterial activity of the ε-PL-HA hydrogels. We reported the biomedical potential of the developed *in situ* forming covalently cross-linked hydrogel scaffolds based on ε-PL and HA for use as novel antibacterial biomaterials for tissue engineering applications, owing to its biocompatibility, sterilizability, and flourishing antibacterial activity against Gram-negative *E. coli* and Gram-positive *S. aureus* strains [25,26].

Despite the promising characteristics, injectable natural biopolymer-based hydrogels still need to be improved as a bone-filling material, as they cannot provide the critical bone-forming capability necessary to promote bone repair and healing and need better structural integrity and mechanical properties [19]. The injectable polymer hydrogels require a suitable bioactive filler to promote osteogenesis effectively [27,28]. Considering that bone is a natural hierarchical biocomposite, there has been a growing trend to develop novel injectable nanocomposite hydrogels by biofunctionalization of injectable conventional hydrogel networks with bioactive inorganic nanofillers such as CaP particles to introduce specialized functional properties (support mesenchymal stem cell differentiation, influence ECM protein adsorption, enhance cell adhesion and tissue formation), mimic the bone's unique nanostructure and composition, thus enhancing bone regeneration capability [29]. Moreover, incorporating CaP nanofillers into conventional hydrogels improves structural integrity, porosity, viscoelastic properties, and degradation rate of the material, making it more efficient as a biomaterial for bone regeneration [29]. Several studies have explored incorporating bioactive HAp nanoparticles into silk fibroin [30], chitosan/alginate [31], bio-mimetic polysaccharide [32] hydrogel networks to form 3D porous scaffolds, and injectable composite hydrogels with enhanced bone tissue regeneration capability and improved mechanical properties. While CaP can initiate bone formation, bioactive CaP fillers-loaded hydrogels are more compatible with biological systems, and the highly swollen 3D hydrogel networks can provide nutrient diffusion to cells, thereby promoting cell adhesion and attachment [33,34]. Moreover, the osteoimmunomodulatory potential of CaP-based bone biomaterials can be further improved by substituting calcium (Ca^{2+}) ions with other biologically relevant ions, such as strontium (Sr^{2+}) ions [35]. As a bioactive element, Sr has gained attention for its capability to promote new bone formation and inhibit bone resorption through Ca-sensing receptor activation and RANKL expression inhibition. It also has angiogenic properties, making it a promising osteoporosis treatment [36]. Introducing Sr^{2+} ions into the HAp structure enhances its bioactivity and osteogenesis ability [37].

To the best of our knowledge, few reports address the development of non-antibiotic nanocomposite hydrogels for multifunctional bone tissue regeneration, which can simultaneously provide bioactivity, biomolecule delivery, and inherent antibacterial activity. For example, *Wang* et al. prepared injectable antibacterial Ag-containing HAp/gelatin methacryloyl hydrogels [38], *Shin* et al. prepared injectable calcium fluoride/alginate nanocomposite hydrogels [39], *Douglas* et al. prepared injectable Zn- and Sr-enriched bioactive glass gellan gum composite hydrogels [40]. So far, there are no studies found on the development and evaluation of injectable nanocomposite hydrogels based on bioactive Sr-substituted HAp (Sr-HAp) and HA and antimicrobial ε-PL for bone tissue engineering applications.

In a recent study, we synthesized Sr-HAp nanoparticles as local delivery vehicles of osteogenic factors. We systemically evaluated its physicochemical properties, *in vitro* Sr^{2+} ion release, and cellular effects on pre-osteoblastic and osteoblastic cell lines [41]. In this study, we used the Sr-HAp as the bioactive inorganic nanofiller for injectable nanocomposite hydrogel fabrication.

This work aims to develop multifunctional injectable nanocomposite hydrogels based on Sr-HAp-loaded covalently crosslinked ε-PL-HA hydrogel network. First, the optimal mass ratios of the Sr-HAp were selected for further systematic investigation based on the nanocomposite hydrogels' injection force and syneresis behavior. Next, we systematically evaluated the impact of the Sr-HAp at various mass ratios of 40 wt%, 50 wt%, and 60 wt% on the physicochemical properties, rheological properties, *in vitro* antibacterial performance, and *in vitro* osteogenic capability of the injectable Sr-HAp-loaded ε-PL-HA nanocomposite hydrogels (Sr-HAp/ε-PL-HA). For the first time, our results demonstrate the developed Sr-HAp biofunctionalized ε-PL-HA hydrogels with the successful incorporation of the Sr-HAp nanofiller up to 60 wt% to create a stiffer hydrogel microenvironment for bone cells synergistically and to provide biocompatibility and cell adhesion while exhibiting prominent *in vitro* inhibitory effect against *S. aureus* and *E. coli*.

2. Materials and methods

2.1. Materials

For the synthesis of Sr-HAp: deionized water (DW, *Adrona Crystal E,* 0.055 μS), calcium carbonate ($CaCO_3$, *Schaefer Kalk*, M = 100.09 g/mol, CAS Nr. 471–34-1), phosphoric acid (H_3PO_4, *"Latvijas ķīmija"*, 75 %, M = 97.99 g/mol, CAS Nr. 7664-38-2), strontium carbonate ($SrCO_3$, *Sigma Aldrich*, ≥ 98 %, M = 147.63 g/mol, CAS 1633-05-2).

For the preparation of hydrogels: hyaluronan (HA, *Contipro*, M = 1.71 MDa, CAS Nr. 9067-32-7), ε-polylysine (ε-polylysine hydrochloride (ε-PL·HCl) *Zhengzhou Bainafo Bioengineering Co., Ltd* (Henan, China), 99 % purity, MW 3500–4500 Da, 25–30 l-lysine residues, water content 6.5 %), N-hydroxysuccinimide (NHS, *Sigma-Aldrich*, 98 %, M = 115.09 g/mol, CAS Nr.6066-82-6), 1-ethyl-3-(3-dimethyl aminopropyl)carbodiimide hydrochloride (EDC, *fluorochem*, 99 %, M = 191.70, CAS Nr. 25,952–53-8).

For the physicochemical characterization: phosphate-buffered saline (PBS tablets, *Sigma-Aldrich*), hyaluronidase (hyaluronidase from bovine tests, 400–1000 units/mg solid, *Sigma Aldrich,* CAS Nr. 37,326–33-3), proteinase K (proteinase K from Tritirachium album, ≥30 units/mg protein, *Sigma Aldrich*, CAS Nr. 39,450–01-6), nitric acid (HNO_3, *Chem-Lab,* 65 %, M = 63.01 g/mol, CAS Nr. 7697-37-2), multielement standard solution 5 for ICP (Sr = 10.00 ± 0.03 mg/L, *Sigma Aldrich*, lot No. BCCB7069).

For the antibacterial studies: *Escherichia coli* (*E. coli*, American Type Culture Collection (ATCC©) 25922™) methicillin-sensitive *Staphylococcus aureus* (*S. aureus*, ATCC© 25923™), extended-spectrum β-lactamase *E. coli* (ESBL *E. coli*, clinically isolated from patients at Riga East Clinical University Hospital, Latvia; ethical committee approval ID: 2-PĒK-4/462/2022), methicillin-resistant *S. aureus* (MRSA, clinically isolated from patients at Riga East Clinical University Hospital, Latvia; ethical committee approval ID: 2-PĒK-4/462/2022), tryptone soya broth (TSB, CM0129, *Oxoid Limited*, Hampshire, United Kingdom), tryptone soya agar (TSA, casein soya bean digest agar, Code: CM0131, *Oxoid Limited*, Hampshire, United Kingdom).

For the cell culture studies: human osteoblast line MG-63 (Cat.No CRL-1427) and mouse preosteoblast cell line MC3T3-E1 subclone 4 (Cat. No CRL-2593) were purchased from American Type Culture Collection (ATCC, Manassas, Virginia, USA), Dulbecco's modified Eagle's medium (DMEM, *Sigma*, Irvine, UK), fetal bovine serum (FBS, *Sigma*, St. Louis, MO, USA), penicillin/streptomycin solution (*Sigma*, St. Louis, MO, USA), alpha-modified Eagle's medium with nucleosides and without vitamin C (α-MEM, without L-ascorbic acid, *Gibco*, Grand Island, NY, USA), trypsin/EDTA (*Sigma*, St. Louis, MO, USA), phosphate-buffered saline (PBS, *Sigma*, Irvine, UK), 3-[4,5-dimethylthiazol-2-yl]-2,5 diphenyl tetrazolium bromide (MTT, *Sigma*, St. Louis, MO, USA), dimethyl sulfoxide (DMSO, Sigma, St. Louis, MO, USA), Alkaline Phosphatase Assay Kit (*Sigma*, St. Louis, MO, USA), Triton X-100 (*Sigma*, St. Louis, MO, USA), bovine serum albumin (BSA, *Sigma*, Irvine, UK), QuickStart Bradford 1× Dye Reagent (*BioRad*, Hercules, CA, USA), human procollagen I DuoSet ELISA kit (*R&D Systems,* Minneapolis, *MN*, USA), human matrix metalloproteinase 1 DuoSet ELISA kit (MMP-1, *R&D Systems,* Minneapolis, MN, USA). Cell viability dyes, SYTO 9 and propidium iodide were supplied by *Life Technologies Corp*. (Eugene, OR, USA).

2.2. Synthesis of Sr-HAp

The Sr-HAp was chemically precipitated in a laboratory reactor (*Power Control-Visc P7, IKA Eurostar, WERKE,* Germany) following the procedure described previously in [41]. Before the synthesis, $CaCO_3$ and $SrCO_3$ were calcined at 1100 °C for 1 h to obtain CaO and SrO, respectively. The amount of added SrO was calculated to yield 3 wt% Sr to the total Sr-HAp synthesis yield. The 0.3 M $Ca(OH)_2$/$Sr(OH)_2$ aqueous suspension was prepared by dispersing the CaO and SrO in DW. The 2 M H_3PO_4 aqueous solution was added to the $Ca(OH)_2$/$Sr(OH)_2$ suspension using an automated dosing system (*TITRONIC® universal, Schott,* Germany). Synthesis temperature (45 °C) and agitator speed (100 rpm) were kept constant throughout the synthesis. By adding the 2 M H_3PO_4 aqueous solution, the pH of the synthesis was reduced to 8. After settling for approximately 20 h, the precipitates were vacuum-filtered through a paper filter. Finally, the Sr-HAp wet precipitates were collected as a paste and stored in a refrigerator at 4 °C until further use. The moisture content of the Sr-HAp paste was determined in a moisture analyzer (*Humidity Analyzer MRS 120–3, Kern,* Germany*)* at 120 °C. The Sr-HAp paste with 3 wt% Sr and a moisture content of 80 % was used to fabricate nanocomposite hydrogels. A detailed physicochemical characterization and *in vitro* biological evaluation of the Sr-HAp containing 3 wt% Sr is provided in our recent study [41].

Table 1
Designation and composition of the tested samples.

Designation	Composition
0 % Sr-HAp	100 % ε-PL-HA (where ε-PL:HA 50:50 wt%)
10 % Sr-HAp	Sr-HAp 10 wt%, ε-PL-HA 90 wt%
20 % Sr-HAp	Sr-HAp 20 wt%, ε-PL-HA 80 wt%
30 % Sr-HAp	Sr-HAp 30 wt%, ε-PL-HA 70 wt%
40 % Sr-HAp	Sr-HAp 40 wt%, ε-PL-HA 60 wt%
50 % Sr-HAp	Sr-HAp 50 wt%, ε-PL-HA 50 wt%
60 % Sr-HAp	Sr-HAp 60 wt%, ε-PL-HA 40 wt%
70 % Sr-HAp	Sr-HAp 70 wt%, ε-PL-HA 30 wt%
80 % Sr-HAp	Sr-HAp 80 wt%, ε-PL-HA 20 wt%
Sr-HAp	Sr-HAp 100 wt%

2.3. Fabrication of injectable Sr-HAp loaded ε-PL-HA nanocomposite hydrogels

The *in situ* forming nanocomposite hydrogels were synthesized *via* EDC/NHS-mediated carboxyl-to-amine cross-linking. The designation and composition of the fabricated Sr-HAp/ε-PL-HA hydrogels are summarized in Table 1.

ε-PL, HA, EDC, and NHS amounts were kept constant for fabricated nanocomposite hydrogels (Table S1). The mass ratio of ε-PL and HA were kept at 50:50 wt% for all Sr-HAp/ε-PL-HA series. The as-synthesized Sr-HAp paste was added to the synthesis media at a mass ratio of 10 wt% to 80 wt% (exact amounts of components for each series are summarized in Table S1). All components were mixed and homogenized using an interconnected syringe technique (*Fisher Scientific*, *BD PlastiPak*™ Syringe with *Luer* Lock, 5 mL) at room temperature (23 °C) following the order depicted in Fig. 1.

The nanocomposite hydrogel fabrication step-by-step process: a) preparation of the first syringe: 0.105 g of the HA powder was dissolved in 2 mL of the DW by rapidly mixing using interconnected syringes. HA aqueous solution, EDC, and NHS were stored in the refrigerator at 4 °C for 24 h; b) preparation of the second syringe: 0.098 g of the ε-PL powder was dissolved in DW by rapidly mixing using interconnected syringes. The amount of the DW added to the ε-PL powder varied depending on the mass ratio of the Sr-HAp paste (Table S1), so the total amount of water in the first syringe was 2 mL; Sr-HAp paste was homogenously dispersed into the as-prepared ε-PL aqueous solution using the same interconnected syringes. The second syringe with ε-PL/Sr-HAp aqueous suspension was stored in the refrigerator at 4 °C for 24 h; c) After 24 h, 0.093 g of the EDC was added into the first syringe (as-prepared HA aqueous solution) and mixed using the same interconnected syringes. Afterward, 0.056 g of the NHS was mixed into the first syringe. The molar ratio of EDC to NHS was set at 1:1. Finally, the aqueous mixture of the pre-activated HA/EDC/NHS in the first syringe and the homogenous aqueous suspension of the ε-PL/Sr-HAp in the second syringe were connected and rapidly mixed for 1 min. The molar ratio of ε-PL to HA was set at 1:0.0026.

2.4. Characterization

Depending on the characterization method, the as-prepared and lyophilized nanocomposite hydrogels were characterized.

The as-prepared nanocomposite hydrogels were fabricated as follows: the precursor mixtures were cast into cylindrical molds (diameter 10 mm, height 5 mm) for uniformity and left to crosslink for 24 h at room temperature (23 °C).

The lyophilized nanocomposite hydrogels were prepared as follows: the as-prepared hydrogels were frozen at −26 °C and lyophilized using a lyophilizer *BETA 2–8 LSCplus* (*Martin Christ*, Germany) at 75 mtorr for 72 h.

For the antibacterial and *in vitro* cell studies, the as-prepared nanocomposite hydrogels were steam-sterilized in an autoclave at 121 °C for 20 min.

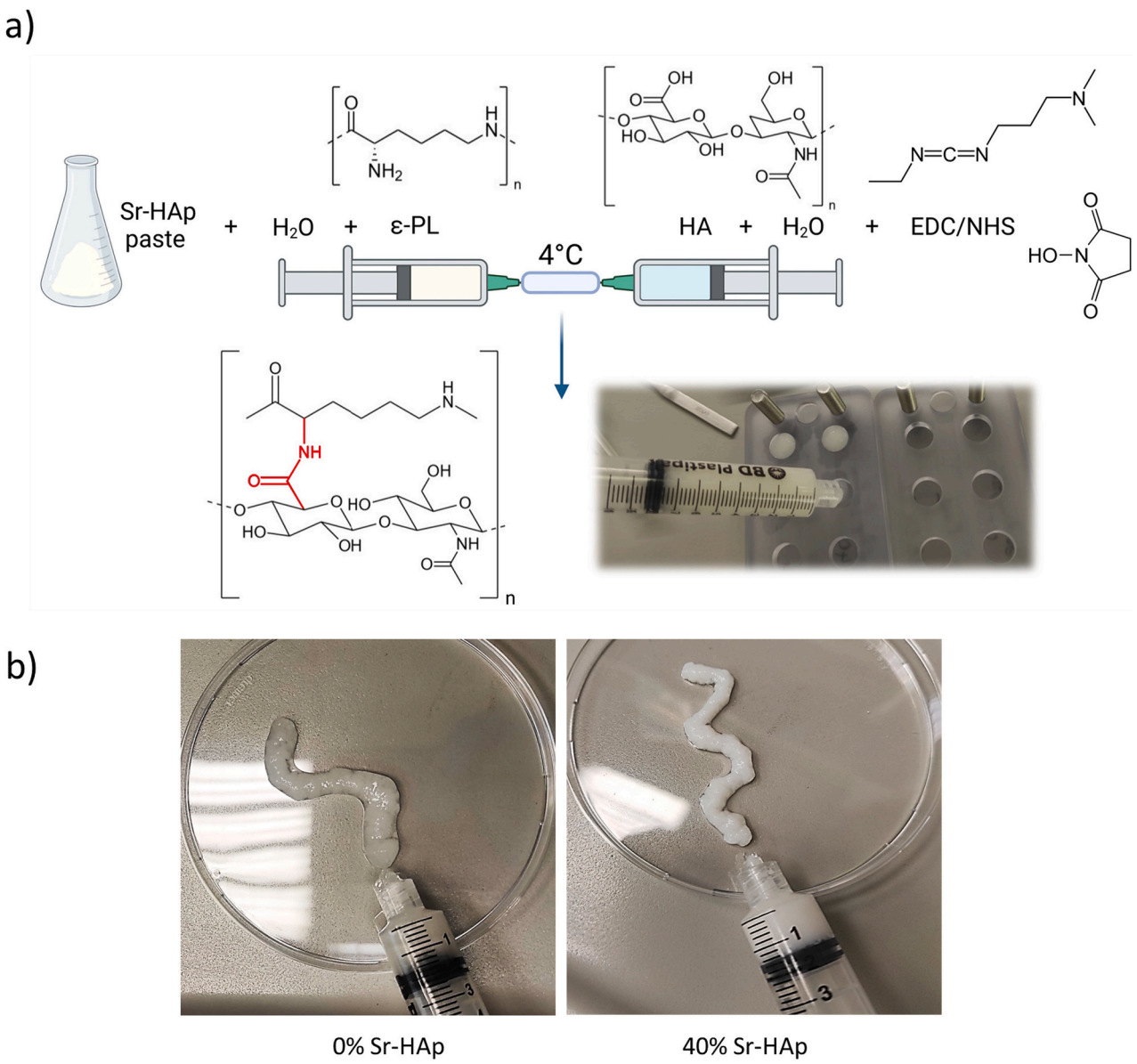

Fig. 1. a) Schematic representation of the synthesis of the nanocomposite hydrogels, b) - digital photos of the as-prepared (on the left) and 3D-molded (on the right) nanocomposite hydrogels (COLOR).

2.4.1. *Injection force*

The injection force of the as-prepared nanocomposite hydrogels was measured by mechanical testing following an analogous method described in [42]. The measurements were performed on an electromechanical universal testing machine (*Model 25ST, Tinius Olsen,* USA). The setup used to determine injection force is shown in Fig. S1. Briefly, the 5 mL syringe (the inner diameter of the tip 1.8 mm) with the as-prepared nanocomposite hydrogel was inserted vertically in a custom-made stand that was inserted into the electromechanical universal testing machine. The syringe plunger was pressed down at a set rate, 1 mm/s, while the applied force was recorded. All measurements were done in triplicate.

2.4.2. *Syneresis*

The syneresis, namely liquid exudation from the gel network during gelation, was determined by placing the as-prepared nanocomposite hydrogels in pre-weighed test tubes (W_E), weighed (W_I) and incubated in a table-top environmental shaker-incubator (*ES-20, Biosan,* Latvia) at 37 °C providing orbital shaking at 100 rpm. After 24 h, the test tubes were opened, the separated water was decanted, and the tubes with the nanocomposite hydrogel were weighed again (W_F). Syneresis was calculated as follows: Syneresis $= (W_I - W_F)/(W_I - W_E) \times 100$ %. All measurements were done in triplicate.

2.4.3. *Rheology*

Time, amplitude, frequency sweep tests, shear rate dependent viscosity, compression, and cyclic strain time sweep tests were chosen for rheological studies. The *Thermo HR-20 Hybrid* rheometer (*TA Instruments,* USA), a 25 mm parallel plate with a gap of 1 mm, was used. Silicone oil was gently applied around the sample to avoid evaporation, and a humidity control trap was used. All tests were performed at 25 °C. The precursor mixture was extruded directly on the rheometer plate for the time sweep tests before complete gelation occurred: a) the precursor mixtures of the nanocomposite hydrogels were extruded on the Peltier plate of the rheometer; b) a parallel plate was slowly lowered toward the nanocomposite hydrogel sample.

The time sweep analysis was performed for 180 min at 0.2 % strain and 1 Hz frequency. For the amplitude and frequency sweep and

compression tests, the precursor mixtures of the nanocomposite hydrogels were extruded into a custom mold (diameter 25 mm) and left to crosslink for 3 min. The amplitude sweep tests were performed in oscillatory mode with a shear strain logarithmically changing range from 0.01 to 1000 % at a constant frequency of 1 Hz. The frequency sweep tests were performed in oscillatory mode varying from 0.01 to 100 Hz at a constant strain of 0.2 % within the linear viscoelastic region (LVR), as experimentally observed for all samples during amplitude sweep experiments. The stiffness of the nanocomposite hydrogels was determined from the amplitude sweep tests as the G' value at 0.2 % strain and 1 Hz frequency. The viscosity-shear rate tests were performed at shear rate values, logarithmically increasing from 0.1 to 500 s^{-1}. The compression tests were performed at 8 N axial force (axial force > dynamic force = 30 %), axial displacement 30 μm, in the frequency range from 0.01 to 16 Hz, and compression storage modulus (E') and compression loss modulus (E'') were monitored. The molecular weight between crosslinks (M_c) of the composite hydrogels was calculated as follows: $M_c = RTd/G'$, where R is the universal gas constant, T is the absolute temperature, and d is the density of the polymer (found experimentally by dividing sample mass with the volume ($d = m/V = m/\pi r^2 h$)), G' is storage module at 1 Hz frequency. Afterward, crosslinking density (q) was calculated: $q = M_w/M_c$, where M_w is the molecular weight of the monomer calculated as follows: $M_w = M_w(HA) + M_w(\varepsilon\text{-}PL)$, where $M_w(HA)$ is the molecular weight of a HA monomer, and $M_w(\varepsilon\text{-}PL)$ is the molecular weight of an ε-PL monomer [43]. The cyclic recovery tests were performed to evaluate nanocomposite hydrogels' recovery after extrusion-like conditions. One cyclic recovery test duration was 130 s, divided into three stages, of which the duration of the first and third was 60 s at a shear rate of 0.1 s^{-1} and the second - 10 s at a shear rate of 350 s^{-1}. All measurements were done in triplicate.

2.4.4. Swelling degree and gel fraction

The swelling degree of the lyophilized and as-prepared nanocomposite hydrogels and the gel fraction of lyophilized nanocomposite hydrogels were determined gravimetrically using an analytical scale (*Kern 770, Kern,* Germany).

To determine the swelling degree, the as-prepared hydrogel cylinders (7 replicates) were weighed (W_D), immersed in 20 mL PBS (pH = 7.4), and incubated at 37 °C with 100 rpm agitation. At specific time points (1, 2, 4, 5, 6, 24, 48 h), the samples were removed from the PBS, the excess liquid was gently shaken off, and the samples were weighed (W_S). The swelling degree (SW) was calculated as follows: $SW = (W_S - W_D)/W_D \times 100$ %.

To determine the gel fraction, the lyophilized nanocomposite hydrogels (5 replicates) were weighed (W_D), immersed in 20 mL PBS (pH = 7.4), and incubated at 37 °C with 100 rpm agitation. After 24 h, the samples were removed from the PBS and lyophilized again. The lyophilized samples were weighed again (W_G), and the gel fraction (GF) was calculated as follows: $GF = W_G / W_D \times 100$ %.

2.4.5. Phase composition

To analyze the phase composition (Fig. S6(a)), the nanocomposite hydrogels were lyophilized as described above, and the Sr-HAp paste was dried at 105 °C for 24 h. Further, the dried Sr-HAp paste, and the lyophilized nanocomposite hydrogels were ground into a fine powder using a pestle. The Sr-HAp and nanocomposite hydrogels' phase composition was evaluated by X-ray powder diffractometry (XRD, *PANalytical AERIS,* Almelo, Netherlands) with Cu Kα radiation (produced at 40 kV and 15 mA). The diffraction data were collected in a 10–70° 2θ range, with a step size of 0.044° 2θ and time per step of 99.45 s. Phases present in the recorded diffraction patterns were identified using a *PANalytical X-Pert Highscore 2.2* software (*Panalytical, Almelo,* Netherlands) and the International Centre for Diffraction Data PDF-2 (ICDD, *Newtown Square,* Pennsylvania, USA) database.

2.4.6. Molecular structure

To analyze the molecular structure (Fig. S6(b) and Fig. S7), the nanocomposite hydrogels were lyophilized as described above, and the Sr-HAp paste was dried at 105 °C for 24 h. Further, the dried Sr-HAp paste, and the lyophilized nanocomposite hydrogels were ground into a fine powder using a pestle. The Sr-HAp and nanocomposite hydrogels' molecular structure was analyzed using the Fourier transform infrared spectroscopy (FT-IR, *Nicolet IS50 FT-IR, Thermo Fisher,* USA) in the attenuated reflectance mode (ATR, *IS50 ATR Nicolet, Thermo Fisher,* USA). Absorbance was measured in the wavenumber range of 400 to 4000 cm^{-1} and at 4 cm^{-1} resolution, 64 scans per sample. In addition, Raman spectroscopy was undertaken using a *Renishaw inVia™ Qontor® Confocal* Raman Microscope (*Renishaw Ltd.*, Gloucestershire, UK) using a Raman 'point and shoot' method. Before beginning measurements, the Raman system was calibrated using an internal silicon reference to 520 cm^{-1}. In acquisition mode, the laser was operated at 10 % power (equal to 5 mW) and focused through an x20 objective over an extended wavenumber scan, 200–1800 cm^{-1}, with 60 s integration time (averaged over 6 collections). Averaged spectra were data-processed by cosmic ray removal.

2.4.7. Microstructure and morphology

This study used micro-computed tomography (μ-CT) as a non-destructive imaging technique to analyze samples. Before scanning, samples were lyophilized. The scans were conducted using a μCT50 cabinet cone-beam μ-CT system (*Scanco Medical AG*, Switzerland) with the following parameters: 55 kVp energy, 109 μA tube current, 1100 ms integration time, and a 4 μm voxel size. Each sample was scanned for approximately 5.4 h. After the scanning process, automated reconstruction of 3D datasets from μ-CT projection data was performed. The visualization module utilized advanced 3D data reproduction techniques, employing high-quality beam tracking algorithms to enhance the analysis of large datasets.

The morphology of lyophilized nanocomposite hydrogels was analyzed by scanning electron microscopy (SEM) *Verios 5 XHR SEM* (*Verios, Thermo Scientific*, USA). The images were generated using secondary electrons at an acceleration voltage of 2 kV. The samples were fixed on aluminum pin stubs with electrically conductive carbon tape.

2.4.8. Enzymatic degradation and ion release

Enzymatic degradation of the as-prepared nanocomposite hydrogels was determined by measuring the remaining weight of the samples upon hyaluronidase treatment (0.025 mg/mL equal to 100 U/sample) over a five-month incubation period. Biodegradation media was prepared by dissolving hyaluronidase powder in PBS (25 mg hyaluronidase added to 100 mL PBS solution) and then diluting the solution 10 times. All samples (5 replicates) were weighed (W_0) before immersion in 10 mL biodegradation media at 37 °C with 100 rpm agitation. The biodegradation media was changed daily, and the weight of the incubated samples was recorded once a week (W_R). The remaining weight (RW) was expressed as a percentage of the sample's initial weight: $RW = W_R / W_0 \times 100$ %.

Enzymatic degradation of the as-prepared nanocomposite hydrogels was also studied in the presence of proteinase K (0.05 mg/mL equal to 12.5 U/sample) over a twelve-day incubation period. Biodegradation media was prepared by dissolving proteinase K powder in PBS (60 mg proteinase K added to 120 mL PBS solution) and diluting the solution 10 times. 5 replicates were weighed (W_0) before immersion in 10 mL biodegradation media at 37 °C with 100 rpm agitation. The biodegradation media was changed daily, and the weight of the incubated samples was recorded once a day (W_R). The remaining weight (RW) was expressed as a percentage of the sample's initial weight: $RW = W_R / W_0 \times 100$ %.

The as-prepared hydrogel cylinders and the Sr-HAp paste were used for ion release measurements. The 5 replicates of each nanocomposite hydrogel series, as well as Sr-HAp paste (20 mg of dry mass), were

weighed in the plastic sample containers, poured over with 20 mL PBS (pH = 7.4), and incubated at 37 °C with 100 rpm agitation. At 1 h, 4 h, 24 h, 1 day, 7 days, 14 days, 30 days, 60 days, and 90 days, in the case of hydrogels, all the PBS, and in the case of Sr-HAp paste - 10 mL of the PBS was removed and replaced with fresh PBS. The amount of released Sr^{2+} and Ca^{2+} ions in the PBS after incubation of the hydrogels and the Sr-HAp paste was measured by an inductively coupled plasma mass spectrometry (ICP-MS; *Agilent 7700×, Agilent Technologies,* Tokyo, Japan). The ICP-MS method was validated before sample analysis regarding the limit of quantification (LOQ), precision, trueness, recovery, uncertainty, stability, and carry-over. The validation results are summarized in Table S2. The stock solution of 0.25 mL concentrated nitric acid (HNO_3, 65 %) was diluted to 50 mL with DW (*A* 0.055 μS/cm, *Adrona Crystal*) was used. The experimental PBS samples were dissolved in 0.5 % HNO_3 aqueous solution and diluted with deionized water. The degree of dilution was optimized before the analysis of each series of samples to ensure that the measured concentration was within the linear range of the calibration curve. The sample measuring parameters were as follows: plasma mode – regular, robust, RF forward power 1300 W, sampling depth 8.0 mm, plasma gas flow 15.0 L/min, carrier gas flow 0.6 L/min, dilution gas flow 0.4 L/min, spray chamber temperature 2 °C, extraction lens 0 *V*, kinetic energy discrimination 3 V.

2.4.9. In vitro antibacterial activity

The long-term antibacterial activity of the sterilized as-prepared nanocomposite hydrogels was assessed using a plate counting method according to CLSI and EUCAST standards with minor modifications, as described in an earlier study [26]. The experiment was performed against four bacterial strains: Gram-negative *E. coli* (reference (ATCC) and clinically isolated antibiotic-resistant (ESBL *E. coli*)) and Gram-positive *S. aureus* (reference (ATCC) and clinically isolated antibiotic-resistant (MRSA)). The tests were performed for extended periods with time control points at 24, 48, 72, and 168 h. First, the bacterial suspensions were prepared in glass tubes with PBS until they reached *McFarland* = 0.5, corresponding to a bacterial concentration of $1.5 \cdot 10^8$ CFU/mL. In the second step, experimental 6-well plates were prepared for each bacterium with positive/negative and three replicates of the sterilized as-prepared nanocomposite hydrogels from each composition. The positive control consisted of 2 mL PBS, and the negative control consisted of 2 mL bacteria suspension in PBS equal to $3 \cdot 10^8$ CFU/mL. The sterilized as-prepared nanocomposite hydrogels were inserted in 2 mL bacterial suspension (at $3 \cdot 10^8$ CFU/mL final concentration). Prepared 6-well plates were tightly sealed with parafilm and incubated for 24 h at 37 °C with 60 rpm agitation. For pre-determined control time points, supernatants were completely extracted from wells, and samples were poured with 2 mL of a freshly prepared bacteria suspension. Finally, surviving bacterial colonies were counted by preparing 6-fold dilutions (1:10 to 1:1000000) and applying the dilution bands on the TSA plate. The TSA plates were dried at room temperature and then incubated at 37 °C for 24 h. The bacterial colonies were counted manually from dilution bands.

2.4.10. In vitro cell studies

Three to five replicate samples of each nanocomposite hydrogel series were analyzed using *in vitro* cell assays. The cylindrical samples of the as-prepared 0 % Sr-HAp, 40 % Sr-HAp, 50 % Sr-HAp, and 60 % Sr-HAp hydrogels with an average weight of 0.055 ± 0.009 g, 0.074 ± 0.008 g, 0.082 ± 0.007 g, and 0.082 ± 0.009 g, respectively, were used for the *in vitro* cell studies.

2.4.10.1. Cell cultures. Human osteoblast line MG-63 (Cat.No CRL-1427) and mouse preosteoblast cell line MC3T3-E1 subclone 4 (Cat.No CRL-2593) were purchased from American Type Culture Collection (ATCC, Manassas, Virginia, USA) and used for biocompatibility testing. MG-63 cells were grown in DMEM supplemented with 100 μg/mL of streptomycin, 100 μg/mL of penicillin, and 10 % (*v*/v) FBS. MC3T3-E1 cells were cultivated in α-MEM cell culture media supplemented with 100 μg/mL of streptomycin, 100 μg/mL of penicillin, and 10 % (v/v) FBS. Cell cultivation was done at 37 °C within a humidified 5 % CO_2 atmosphere. Cells were detached and passaged using 0.25 % trypsin/EDTA. Both cell lines were used for proliferation and alkaline phosphatase (ALP) activity assays. Collagen production and MMP-1 secretion were assessed for MG-63 cells.

2.4.10.2. Cell proliferation assay. A proliferation assay was performed in the human osteoblast cell line MG-63 and mouse preosteoblasts MC3T3-E1. The as-prepared hydrogels were washed two times with sterile PBS (pH 7.4) and once with cell culture media and placed in 48-well cultivation plates. MG-63 osteoblasts and MC3T3-E1 preosteoblasts ($5 * 10^3$ cells per well) were seeded on the hydrogels. Plates were incubated for 2, 5, and 7 days. After incubation, the media was removed, and the hydrogels were transferred to a new cultivation plate. The cell proliferation, both in the hydrogels and on the cultivation plate surface surrounding the hydrogels, was quantified using an MTT reduction assay: (a) 0.5 mL of 0.5 mg/mL MTT solution in 5 % serum-containing medium was added to each well, (b) plates were incubated for 3 h at 37 °C and 5 % CO_2 to allow the formation of insoluble formazan precipitates due to the metabolic activity of viable cells, (c) 0.45 mL of DMSO was added, (d) the plate was incubated for 30 in case of cells grown on the plate surface in presence of biomaterial and 2 h in case of hydrogel samples at room temperature with gentle shaking to dissolve the formazan precipitate, (e) the absorption was measured at 570 nm using an *Infinite Pro 200* microplate reader (*Tecan,* Austria). Blank wells without cells were used for the background measurement. Cells grown on the cultivation plate surface without the biomaterials were used as controls.

2.4.10.3. Alkaline phosphatase assay. The alkaline phosphatase (ALP) activity after 3, 5, and 7 days in the osteoblast and the pre-osteoblast cultures was measured using The Alkaline Phosphatase Assay Kit. Cells were seeded on the hydrogels in the 48-well plates as described in Section 2.4.10.2. Cells cultivated on the surface of a 48-well cultivation plate were used as controls. The plates were incubated at 37 °C, 5 % CO_2 for 3, 5, and 7 days; half of the culture media was changed every 3 days. After the incubation, the media was aspirated. The hydrogels were washed with 0.5 mL of PBS and transferred to the new 48-well plate to prepare lysates from cells grown in the hydrogels and on the cultivation plate in the presence of the hydrogels. Cells were lysed with 0.5 mL of 0.2 % Triton X-100 aqueous solution for 20 min with shaking at room temperature. ALP activity was measured according to the manufacturer's protocol: (a) a reaction working reagent containing 200 μL assay buffer, 5 μL 0.2 M Mg acetate, and 2 μL 1 M pNPP was prepared, (b) 30 μL of cell lysate was mixed with 170 μL of the working reagent, (c) optical density (*OD*) at 405 nm was measured immediately after mixing (OD_{0min}) and after 50 min incubation (OD_{50min}) using the microplate reader. Incubation time was prolonged compared to standard ALP activity assay protocol due to the relatively low activity in the cell lysates. Tartrazine supplied with the kit was used as a calibrator (OD_{cal}), and water was used as the blank (OD_{blank}). The following equation was used to calculate *ALP* (IU/mL):

$$ALP = ((OD_{50min} - OD_{0min}) \times RnxVol \times 35.3)/((OD_{cal} - OD_{blank}) \times SampleVol \times T),$$

where *RnxVol* is the reaction volume, *SampleVol* is the sample volume, and *T* is the incubation time. The total protein content in the cell lysates was determined using *QuickStart Bradford* 1× Dye Reagent and BSA as a standard. ALP activity was expressed as IU/mg protein.

2.4.10.4. Secretion of pre-collagen I and MMP-1. MG-63 osteoblasts were seeded on the hydrogels in the 48-well plates as described in

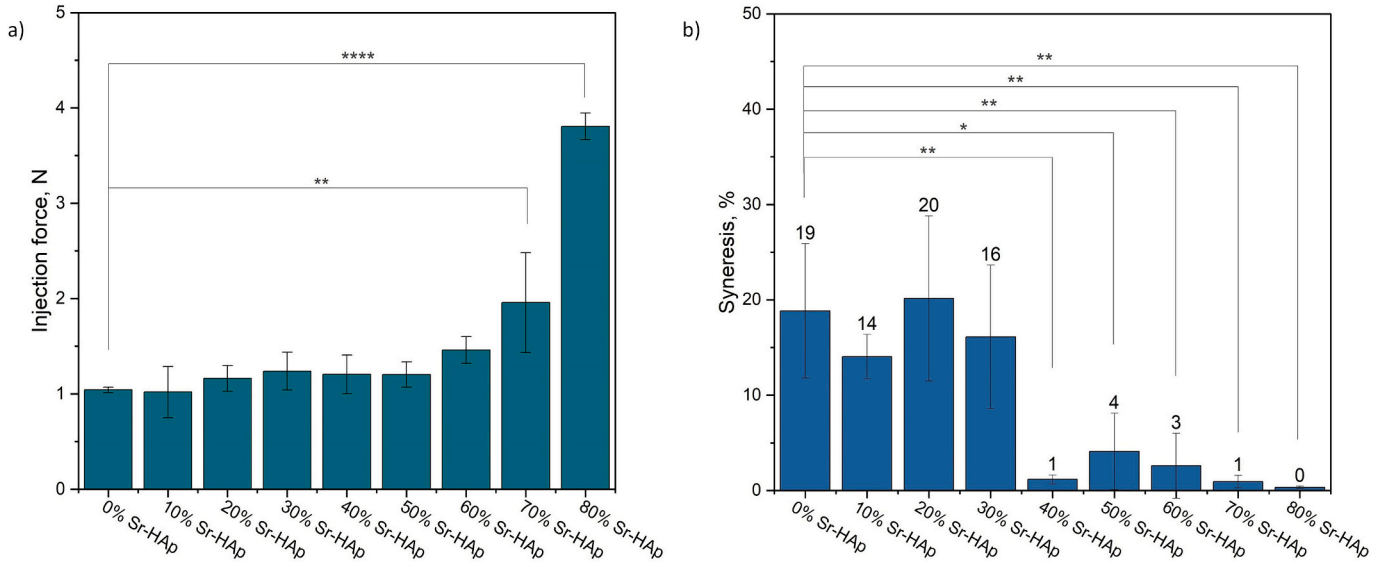

Fig. 2. The injection force (a) and the syneresis level (b) of the Sr-HAp-loaded ε-PL-HA nanocomposite hydrogels (ANOVA: * - for $p < 0.05$, ** - for $p < 0.01$, *** - for $p < 0.001$, **** - for $p < 0.0001$, $n = 3$) (COLOR).

Section 2.4.10.2. Cells cultivated on the surface of a 48-well cultivation plate were used as controls. The plates were incubated at 37 °C, 5 % CO_2 for 7 days, and half of the culture media was changed every 3 days. Media were collected for analysis after 2, 5, and 7 days of hydrogel cultivation. The secretion of pro-collagen I and MMP-1 in the culture media was quantified using ELISA immunoassays employing *DuoSet Human* pro-collagen I alpha 1 and MMP-1 ELISA kits (*R&D Systems*, USA), following the manufacturer's recommendations. Standard dilutions of pro-collagen I and MMP-1 were used to generate the standard curve and calculate the concentrations of both analytes in the culture media. The pre-collagen I to MMP-1 ratios were calculated for all formulations.

2.4.10.5. Live/dead staining. Cells were seeded on the hydrogels in the 48-well plates as described in Section 2.4.10.2. Cells cultivated on the surface of a 48-well cultivation plate were used as controls. The plates were incubated at 37 °C, 5 % CO_2 for 5 and 7 days. After cultivation, the media was discarded, and samples were washed with PBS. A mixture of fluorescent cell viability dyes (5 μM SYTO 9 dye and 30 μM propidium iodide) was added to the samples and incubated for 15 min at 37 °C, 5 % CO_2 in the dark. After incubation, samples were washed with PBS and imaged using *Leica DMI400B* inverted fluorescence microscope.

2.4.11. Statistical analysis

All results were expressed as the mean value ± standard deviation (SD) of at least three independent samples. The significance of the results was evaluated using One-way ANOVA with the significance level set at $p < 0.05$ (ns - > 0.05, * - for $p < 0.05$; ** - for $p < 0.01$; *** - for $p < 0.001$; **** - for $p < 0.0001$). Cell studies data processing, visualization, and statistical analysis were performed using GraphPad Prism 9 software.

3. Results and discussion

3.1. Injection force and syneresis

For hydrogels to be injectable, transporting the sol or the pre-gel to a target site through an injection device is required [44]. Thus, injectability is related to the ease of administration. Knowing how much force (injection force) is needed to push the hydrogel out at a given injection rate is essential. As discussed, we aimed to replicate bone composition, namely, the polymeric phase intercalated by the inorganic phase [16]. Thus, the addition of the inorganic filler, the Sr-HAp, was expected to affect the injection force of the ε-PL-HA hydrogels due to the change in the viscous properties [45]. Therefore, the injection force was measured for each series of the fabricated Sr-HAp/ε-PL-HA to define the appropriate amount of the Sr-HAp without compromising the injectability of the nanocomposite hydrogels. The results are shown in Fig. 2(a).

The force measured at the syringe plunger depends on the syringe and needles employed [46]. It has been reported that gauge sizes from 10 (inner diameter 2.69 mm) to 16 (inner diameter 1.19 mm) are appropriate for orthopedic procedures such as filling bone lesions and cracks [47]. Since the inner diameter of the syringe tip (1.8 mm) corresponds to these dimensions, the injection force measurements were done without a needle. As described in the literature, the injection force should be below the acceptable limit of manual injectability for subcutaneous injection, which is 30 N [48]. The measured injection forces for all the fabricated Sr-HAp/ε-PL-HA series are under 5 N. Therefore, we can assume all tested nanocomposite hydrogels are manually injectable in a clinical setting. The measurements show a slight increase in injection force while increasing the Sr-HAp mass ratio from 0 % to 70 % and a steep increase for 80 % Sr-HAp.

The phenomenon of syneresis means macroscopic shrinkage and liquid exudation from the gel network after gelation [49]. This is an undesirable feature for injectable biomaterials. It can lead to gel size and shape changes and, thus, to the inefficient filling of bone defects [50]. The degree of syneresis of the fabricated nanocomposite hydrogel series is summarized in Fig. 2(b). The degree of syneresis of the Sr-HAp/ε-PL-HA decreased with increasing the Sr-HAp mass ratio. Thus, Sr-HAp enhanced the nanocomposite hydrogel stability and acted as the syneresis inhibitor. To explain the decrease of the syneresis by increasing the Sr-HAp mass ratio, the hydrophilicity of the Sr-HAp particles due to the surface [OH] groups should be considered [51,52]. The [OH] groups can form hydrogen bonds, thus limiting the movement of polymer chains and lowering the syneresis of the nanocomposite hydrogels. The most optimal Sr-HAp/ε-PL-HA ratios were selected for further studies based on the described injectability and syneresis results. The syneresis results indicate that the hydrogels with a higher Sr-HAp mass ratio (≥40 %) could be more favorable for use as injectable biomaterials. On the other hand, the injectability results show that increasing the Sr-HAp mass ratio in the nanocomposite hydrogels to 80 % requires a higher injection force, which is undesirable. Thus, the nanocomposite

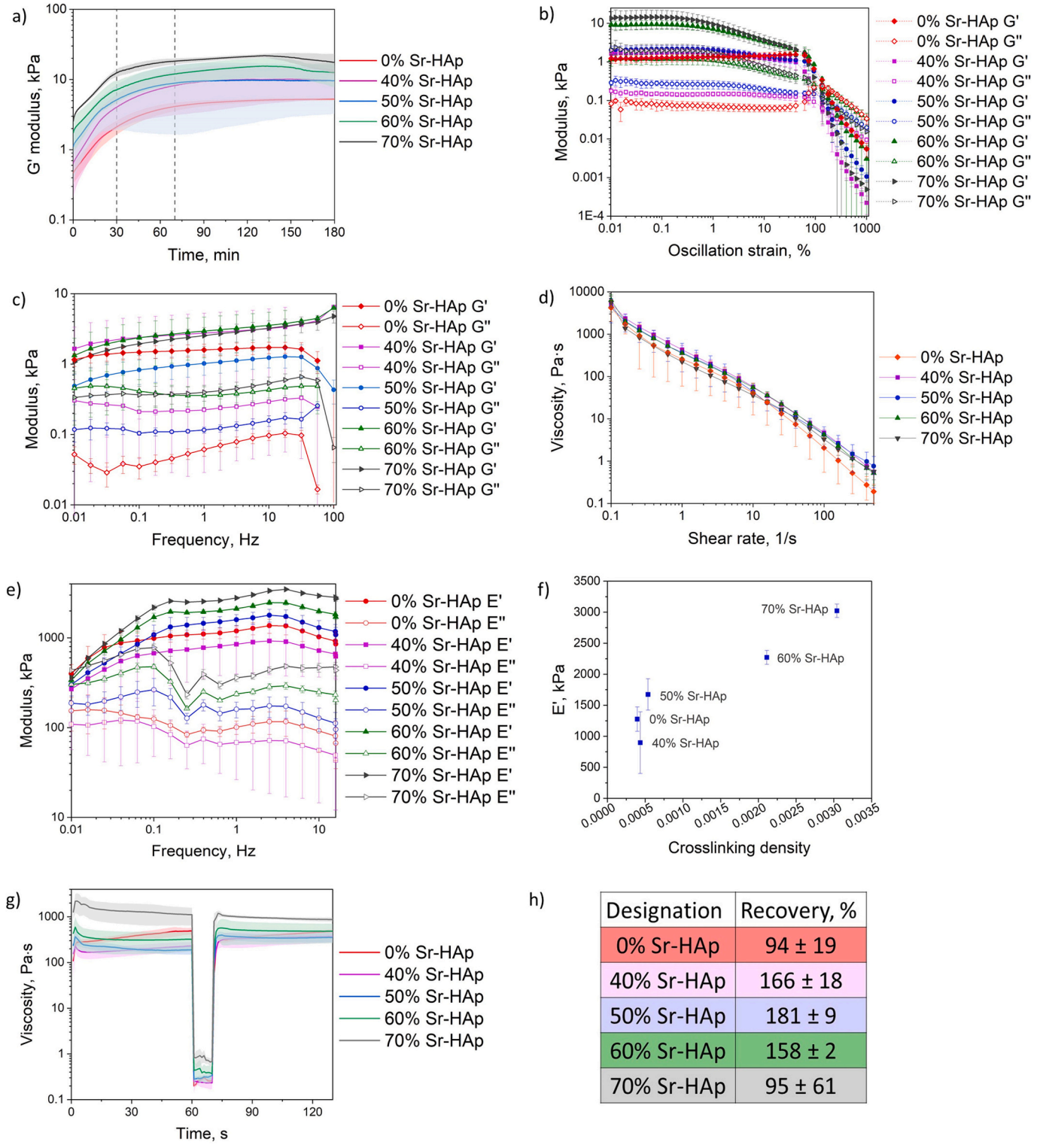

Designation	Recovery, %
0% Sr-HAp	94 ± 19
40% Sr-HAp	166 ± 18
50% Sr-HAp	181 ± 9
60% Sr-HAp	158 ± 2
70% Sr-HAp	95 ± 61

Fig. 3. The rheological characterization of the nanocomposite hydrogels: a) time sweep curves, b) amplitude sweep curves, c) frequency sweep curves, d) viscosity – shear rate curves, e) compression curves, f) correlation between compression storage moduli (*E'*) (extracted from compression curves at 1 Hz) and calculated crosslinking density values, g) cyclic strain time sweep curves, and h) calculated viscosity recovery rates (COLOR).

hydrogels with 40, 50, 60, and 70 % of the Sr-HAp were chosen for further evaluation.

3.2. Rheology

The rheological properties of injectable hydrogels are essential to predict their viscoelastic performance during and after injection and whether they resist tension forces due to movements in the injected area [53]. Optimally, the viscosity of the injectable gel should be low in the initial stage but increase rapidly with time to ensure an easy injection and, subsequently, a quick formation of bulk hydrogel to avoid its outflow to the surrounding tissues [54]. Gelation time is one of the most

critical parameters when applying hydrogels as injectable biomaterials. The dynamic process of gelation time should include mixing the components, injection, and complete filling of the target sites and the final gelation of the hydrogel [55]. Rheological oscillation time sweep analysis shows the storage moduli (*G'*) dependence on time. This allows us to predict the time needed for the hydrogels to transit from fluid flow-like behavior to solid elastic behavior, namely, the total gelation time. The time sweep curves are summarized in Fig. 3(a).

Usually, the *G'* and *G″* curve crossover point indicates the gelation point of the hydrogels [56]. However, throughout the tests, *G'* was greater than that of *G″* for all formulations, indicating the elastic nature of the hydrogels over their viscous nature. This can be explained by forming a gel-like structure while mixing the reagents. As the EDC and NHS are added to the HA solution, the [COOH] groups of the HA are activated, forming an O-acylisourea active ester that reacts with nearby [OH] groups, generating intermolecular cross-links [57,58]. Consequentially, we used this test to determine the stability of the hydrogels. Namely, the hydrogels were considered stable when the *G'* value reached a plateau. The time sweep tests were performed for 3 h to observe the onset of the stable value of *G'*. It can be argued that the formulations were completely gelled within 30–70 min, depending on the Sr-HAp mass ratio. It has been claimed that the optimal gelation time for injectable hydrogels for bone-filling applications is 5 min [59]. Although this time is significantly longer in our case, the gelation or curing time, in our case, gives sufficient time for mixing the components before injection.

Determination of the LVR plateau region and its limits is crucial for further rheological studies and inferring interconnections and dominance in the sample structure. Thus, the amplitude sweep tests within a constant frequency value of 1 Hz were performed [60]. The amplitude sweep curves are summarized in Fig. 3(b). For all Sr-HAp/ε-PL-HA series, *G' > G"* indicating solid-like material characteristics, namely, the dominance of elasticity over viscous nature, is valid until the crossover point, *i.e.,* until matrix transition occurs [61,62]. This is true for all Sr-HAp/ε-PL-HA series and is mainly predetermined by intermolecular cross-links in the composite structure [56]. The amplitude sweep curves of the 0 % Sr-HAp hydrogels coincide with our earlier study [25]. A relatively high ratio between storage (*G'*) and loss (*G″*) moduli and narrow LVR from 0.1 to 0.5 % and crossover points at an oscillatory strain of ~200 % indicates chemical entanglement dominance in the hydrogel matrix. The curves of the Sr-HAp/ε-PL-HA hydrogels show that adding Sr-HAp has tipped the balance where physical interactions dominate and well-defined LVR regions (0.01–1 %) were observed. Moreover, the addition of the Sr-HAp nanoparticles caused an increase in storage modulus (*G'*). The formation of the physically crosslinked network through electrostatic interactions between the Sr-HAp and the functional groups of ε-PL and HA could explain this. Namely, electrostatic bonds might have been formed either by the SrHAp *a(b)*-planes (Ca^{2+} ions) interaction with negatively charged dissociated carboxyl groups [COO^-] of the HA or through the SrHAp *c*-planes (PO_4^{3-} ions and OH^- ions) interaction with positively charged amino groups [NH_3^+] of the ε-PL [63]. Furthermore, it has been reported that adding and the mass ratio of the inorganic phase might affect stiffness moduli at lower strain values within LVR [25]. The stiffness moduli values in the LVR region increased with increasing the Sr-HAp mass ratio. Up to 50 % Sr-HAp, no statistically significant effect was observed on the stiffness moduli, and the value remained at 1–2 kPa. However, when the mass ratio of the Sr-HAp reached 60 % and 70 %, the stiffness moduli increased to 9 ± 2 kPa and 14 ± 7 kPa, respectively (Fig. S2). A rapid decrease in storage moduli (*G'*) at ~200 % indicates the final matrix transition from solid-like to liquid-like.

The frequency sweep tests were performed at a constant strain value of 0.2 % (defined as a stable strain value within the LVR for all tested samples) (Fig. 3(c)). The nanocomposite hydrogels did not break down within the experimental frequency range. For all compositions, storage (*G'*) and loss (*G″*) moduli remained at the same level, suggesting that the *G'* and *G″* values were relatively independent of the frequency [56]. No transitions or crossover points were observed for the fabricated hydrogels, indicating permanent chemical crosslinking, which correlates with the time sweep test results (Fig. 3(a)).

The shear rate-dependent viscosity tests assessed the dependency of the viscosity of the hydrogels on the applied shear rate to determine the tendency of the hydrogels to flow [56]. Shear-thinning behavior plays a crucial role in the injectability and syringeability of the viscous system. For all tested compositions, viscosity values rapidly decreased as the shear rate increased, confirming that the fabricated hydrogels have shear-thinning behavior and possess injectability (Fig. 3(d)).

Overall, the rheology results suggest that the obtained nanocomposite hydrogels are at least partly characterized by the "gelation first and injection later" features, which offer advantages such as minimization of leakage after injection and efficient adaptation to complex irregular bone defect sites [55]. As described, HA partially intermolecular cross-links upon adding EDC and NHS and forms a gel before injection, which meets the conditions of shear-thinning hydrogels. However, complete cross-linking to create a stable covalently crosslinked hydrogel occurs after injection, *i.e.*, *in situ* gelation. Thus, the hydrogels show the *in-situ* gelation and the shear-thinning characteristics.

The compression tests assessed the dependency of the compression storage (*E'*) and compression loss (*E″*) moduli as a function of frequency under constant axial force compression to simulate the physiological conditions of the human body and to examine the viscoelastic properties of the composite hydrogels in such conditions (Fig. 3(e)). Similar *E'* and *E″* curves were obtained for all tested compositions. However, slightly higher *E'* and *E″* values for the hydrogels with higher Sr-HAp mass ratios could be related to higher resistance to spread in the lateral direction. The *E'* and *E″* curves did not cross over the entire frequency range, indicating a stable, strong, chemically crosslinked polymer network. Generally, the hydrogels proposed for bone tissue regeneration have compression storage modulus ranging from 100 kPa to several MPa [64–66]. Regardless of the composition, the measured compression storage moduli of the nanocomposite hydrogels fall within this region. Thus, we can conclude that the developed hydrogels are suitable for bone tissue regeneration. It should be noted that they are not aimed for load-bearing bone application. Still, they should maintain nutrition transport, possess porosity for cell migration, retain structural integrity, and mimic the extracellular matrix. In addition, the compression storage moduli (*E'*) are plotted as a function of cross-linking density (*q*) (Fig. 3(f)). The *E'* increased with the *q,* which is higher for nanocomposite hydrogels with a higher Sr-HAp mass ratio. A higher cross-linking density leads to lower chain flexibility and, thus, lower uptake and swelling degree. Moreover, these results show that adding Sr-HAp nanoparticles can increase the cross-linking density of composite hydrogels through interaction with the hydrogel matrix, *e.g.*, forming hydrogen bonds and, thus, enhancing the stiffness of the hydrogel [67,68].

Next, the cyclic strain time sweep studies were performed (Fig. 3(g)). This is crucial for extrusion and injectability applications, as the material should overcome stress and retrieve the before-stress properties [61]. The nanocomposite hydrogels were alternately subjected to low and high shear rates to simulate the injection through a syringe. As a result, viscosity recovery rates of the hydrogels with and without Sr-HAp showed recovery ability in the 94–181 % range (Fig. 3(h)). Thus, the hydrogels can survive injection/extrusion-like conditions and recover their structure. An increase in the viscosity over 100 % occurs because the hydrogels are still undergoing gelation, so the viscosity continues to increase throughout the test. However, nanocomposite hydrogels with 70 % Sr-HAp showed the lowest recovery rate of 95 ± 61 % (excluding 0 % Sr-HAp, which is used as a reference). They do not fully recover their structure after the applied stress. The significant standard deviation (61 %) indicates that the 70 % Sr-HAp nanocomposite hydrogel recovery is relatively unpredictable and can be as low as 34 %. Therefore, further studies were conducted only on the 40 % Sr-HAp, 50 % Sr-HAp, and 60

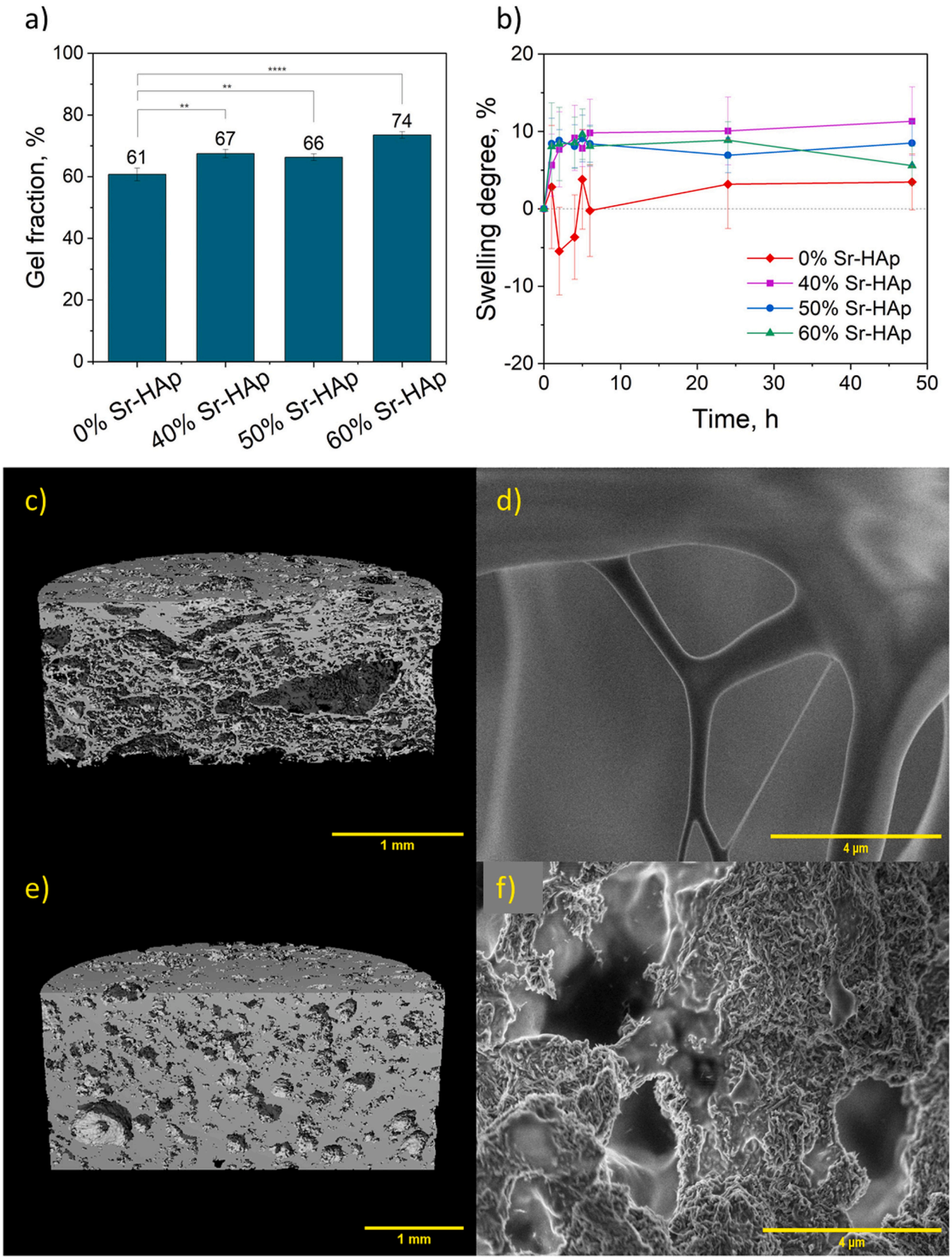

Fig. 4. The gel fraction (a) and the swelling degree (b) of the Sr-HAp-loaded ε-PL-HA nanocomposite hydrogels (ANOVA: * - for $p < 0.05$, ** - for $p < 0.01$, *** - for $p < 0.001$, **** - for $p < 0.0001$, $n = 5$), μ-CT cross-section images of the (c) 0 % Sr-HAp and (e) 60 % Sr-HAp, and the SEM images of the (d) 0 % Sr-HAp and (f) 60 % Sr-HAp at 25 kX magnification (COLOR).

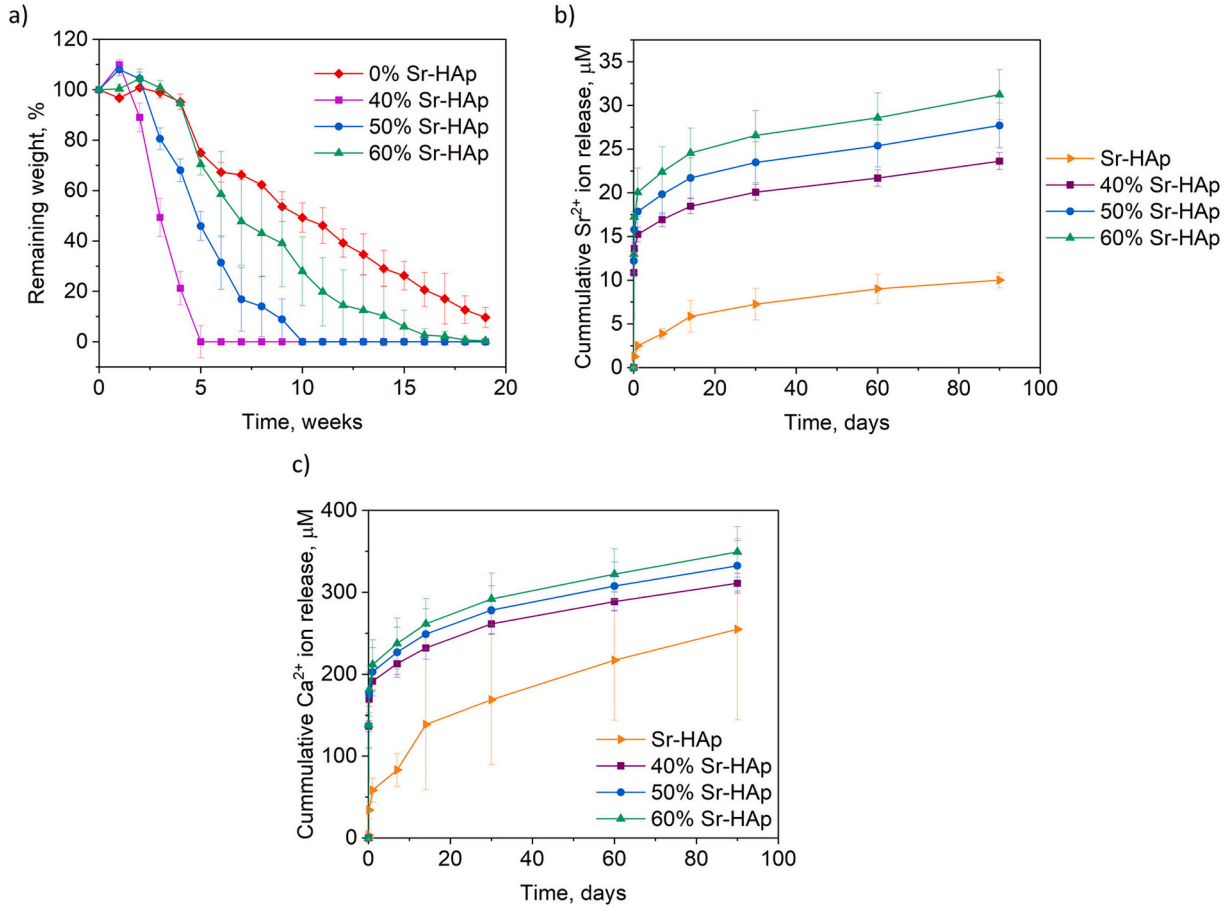

Fig. 5. The enzymatic degradation of the Sr-HAp-loaded ε-PL-HA nanocomposite hydrogels by hyaluronidase (a) and cumulative Sr^{2+} (b) and Ca^{2+} (c) ion release from the as-prepared Sr-HAp-loaded ε-PL-HA nanocomposite hydrogels and the Sr-HAp paste in PBS for up to 90 days ($n = 5$) (COLOR).

% Sr-HAp hydrogels, and the 0 % Sr-HAp hydrogels were used as the reference.

3.3. Gel fraction and swelling degree

The cross-linked fraction of hydrogel is the gel fraction, providing information on cross-linking efficiency and degree. The unreacted fraction can be dissolved and removed, while the crosslinked part, namely the gel fraction, remains. As shown in Fig. 4(a), the gel fraction of the lyophilized nanocomposite hydrogels increased with increasing the Sr-HAp mass ratio. According to synthesis parameters, all nanocomposite hydrogel series were fabricated with constant crosslinking agent concentrations (Table S1). We assume that the slight increase in the crosslinked gel fraction is associated with the Sr-HAp interaction with ε-PL and HA macromolecules. Thus, during the *in-situ* formation of the chemically crosslinked nanocomposite hydrogels, the physically crosslinked network was simultaneously formed *via* electrostatic interactions between charged Sr-HAp and free non-crosslinked functional groups of ε-PL and HA. *Svarca* et al. observed the same effect of CaP addition on the crosslinking efficiency of the HA hydrogels [69]. They attributed this to the influence of the added CaP particles on the distances between the HA chains. Namely, as the particles fill the empty spaces between the polymer chains, the chains are brought closer to each other, allowing crosslinking to occur more effectively. Moreover, the increase in the mass ratio of Sr-HAp was at the expense of the total ε-PL-HA mass ratio (Table S1). Thus, the hydrogels with a higher Sr-HAp mass ratio contain less polymer, which remains free. Accordingly, by removing this unreacted part of the polymers, the total hydrogel weight is less altered. As demonstrated in Fig. S3, the swelling degree of the lyophilized Sr-HAp/ε-PL-HA hydrogels decreases with increasing the Sr-HAp mass ratio, and these results are in good agreement with the gel fraction analysis (Fig. 4(a)). Thus, higher swelling capacity is associated with a lower gel fraction and crosslinking density. The lyophilized nanocomposite hydrogels exhibited fast-swelling ability, reaching an equilibrium swelling degree of ~500–750 % after 1 h. The 0 % Sr-HAp hydrogels reveal a significantly higher swelling degree, reaching the equilibrium swelling rate at 2000 % after 4 h. In general, the chemical composition, the network structure, and the crosslinking density determine the swelling degree of the hydrogels [70]. The high binding affinity of the water molecules of the ε-PL-HA hydrogels and the Sr-HAp/ε-PL-HA nanocomposite hydrogels are primarily associated with the presence of polar hydrophilic functional groups such as primary [NH_2] groups of the ε-PL, [OH] and [COOH] groups of the HA, and [OH] groups of the Sr-HAp. We assume that the increase of Sr-HAp mass ratio in hydrogels introduces new hydrogen bonds and physical crosslinking networks through electrostatic interactions into the hydrogel network, which can limit the free movement of the non-crosslinked part of ε-PL-HA hydrogel. As the Sr-HAp mass ratio is relatively high, the spacings between the crosslinks of the nanocomposite hydrogel network become significantly smaller. In other words, Sr-HAp particles limit the movement of polymer chains and reduce swelling. Accordingly, hydrogels with a smaller mesh size exhibit a lower swelling degree [69]. Moreover, in the case of lyophilized hydrogels, the microstructure significantly influences the degree of swelling. Namely, the amount of retained liquid is related to the porosity of the hydrogels. As shown in Fig. 4(c-f) and described in Section 3.4, the porosity of the ε-PL-HA hydrogels significantly decreases with the addition of the Sr-HAp.

Considering that the hydrogels will be used non-lyophilized, the

degree of swelling of the as-prepared hydrogels was determined and is shown in Fig. 4(b). The as-prepared hydrogels were pre-swollen due to the water added during the preparation. Thus, the degree of swelling is low (up to 10 %). After 5 h, the hydrogels reached a swelling equilibrium, indicating the dimensional and structural stability of the hydrogels due to their pre-swollen form. This observation is beneficial, as in the case of injectable hydrogels, the swelling must be controlled to avoid undesirable compression on the surrounding tissues [71]. Hydrogels without the Sr-HAp did not swell. The swelling degree increased with the addition of the Sr-HAp. However, no changes were observed when the Sr-HAp mass ratio was increased. This could be explained by the differences in the water content of the as-prepared hydrogels (Table S1). The as-prepared 0 % Sr-HAp hydrogel has the highest water content and exhibits a lower swelling degree than the Sr-HAp-loaded nanocomposite hydrogels.

3.4. Microstructure and morphology

A recent review article emphasizes the importance of physically incorporated pores for medical applications of hydrogels. Generally, tissue engineering scaffolds mimic normal tissue development processes, allowing cells to formulate their microenvironment. Ideally, scaffolds have a 3D, highly porous structure with an interconnected pore network to facilitate the diffusion of cells/tissues, nutrients, metabolic wastes, and paracrine factors [72].

Thus, the μ-CT and SEM were used to evaluate the microstructure of the fabricated hydrogels (Fig. 4(c-f)). The pores in the ε-PL-HA hydrogels are formed *in situ* by bubbles trapped in the hydrogel. As the HA and ε-PL are chemically crosslinked with EDC/NHS, the CO_2 bubbles are formed during the activation of the HA carboxyl groups [25]. The hydrogel gelation time is too short for the bubbles to escape the hydrogel matrix, leaving a porous structure (macropores up to 1 mm) [73]. Since these are closed pores, such porosity is undesirable, as it can adversely affect mechanical properties and lead to incomplete bone defect filling. However, it should be noted that before analysis, the samples were lyophilized, and the drying process may have caused artifacts in the hydrogel structure, giving false information [74]. In the case of lyophilization, the primary cause of artifacts is the formation of ice crystals upon freezing [75]. Still, the tendency for porosity and pore sizes to decrease with increasing the Sr-HAp mass ratio was observed. According to μ-CT measurements, the porosity of the hydrogels decreased in the following order: 0 % Sr-HAp (approx. 82 %) > 40 % Sr-HAp (approx. 49 %) > 50 % Sr-HAp (approx. 45 %) > 60 % Sr-HAp (approx. 39 %). Adding the Sr-HAp improves the structural and mechanical integrity of the ε-PL-HA hydrogels.

The SEM images reveal that the Sr-HAp is homogeneously dispersed throughout the hydrogel as a few hundred nm long needle-shaped particles (Fig. 4(f)). However, since the Sr-HAp nanoparticles are embedded in a polymer matrix, they are exposed to the surrounding environment, such as physiological solutions, cell environment, *etc.*, in separate areas.

3.5. Enzymatic degradation and ion release

HA hydrogels in physiological environments degrade by hydrolysis and enzymatic hydrolysis due to naturally occurring hyaluronidase and reactive oxygen species [76]. In turn, ε-PL is degraded by hydrolytic or proteolytic enzymes (proteases), which cleave the peptide bonds between the lysine residues in ε-PL [77]. Thus, the weight loss of the hydrogels by the enzymatic degradation as a function of soaking time in PBS containing hyaluronidase and proteinase K was evaluated, and the results are reported in Fig. 5(a) and Fig. S4, respectively.

The hydrogels swell and degrade concurrently when exposed to the degradation media, accompanied by disruption of their original structure as observed by SEM analysis (Fig. S5). Namely, as the hydrogel swells, the mesh size becomes larger, allowing liquid to diffuse in and out of the hydrogel [78]. However, as the as-prepared hydrogels were pre-swollen upon synthesis, all samples underwent mass loss over time without significant swelling. Hyaluronidase (Fig. 5(a)) treatment promoted little to no degradation of the nanocomposite hydrogels during the first weeks. The 0 % Sr-HAp hydrogels were degraded at a lower rate than the nanocomposite hydrogels. The nanocomposite hydrogels with the lowest Sr-HAp mass ratio (40 % Sr-HAp) showed the fastest enzymatic degradation and degraded fully in 5 weeks. This could be explained by the lower fraction of the polymer used to prepare the hydrogels [58]. Furthermore, the higher Sr-HAp mass ratio led to a lower degradation rate of the nanocomposite hydrogels. This could be due to lower porosity with an increased Sr-HAp mass ratio. Higher porosity favors water absorption (higher swelling degree) and, thus, increases the degradation rate. Another explanation could be related to the acidic nature of the ε-PL-HA hydrogels (approx. pH 5). Degradation of the hydrogels is expected to be accompanied by the release and accumulation of acidic degradation products [79]. This autocatalytic effect can contribute to the dissolution of the Sr-HAp. In turn, the dissolution of the Sr-HAp is associated with a local pH increase. It has been reported that even a slight increase in the pH value enhances the hydrogels' stability, significantly prolonging the degradation rate [80]. The 50 % Sr-HAp and 60 % Sr-HAp hydrogels were degraded within 10 and 19 weeks.

In the case of the proteinase K treatment (Fig. S4), weight loss was observed after the first day, suggesting rapid degradation of the hydrogels. The initial weight loss was higher for the 0 % Sr-HAp hydrogels (approx. 20 %), while it was about the same level for the Sr-HAp-loaded nanocomposite hydrogels (5–10 %). The weight loss differences among various compositions might be explained by simultaneous degradation and water uptake or swelling. As described in Section 3.3., in the case of the as-prepared hydrogels, swelling (swelling degree in PBS up to 10 % at 24 h) was observed only in the case of the Sr-HAp-loaded nanocomposite hydrogels. Hence, the Sr-HAp-loaded nanocomposite hydrogels have a lower degradation rate than their Sr-HAp-free counterparts. In addition, the higher porosity of 0 % Sr-HAp hydrogels enables more efficient diffusion of liquids inside the samples, which may also contribute to their degradation. Afterward, a slight increase in weight was observed, followed by a plateau for the rest of the experiment (up to twelve days) for all compositions. Given that proteinase K hydrolyzes peptide bonds, it is expected that the mass loss mainly resulted from the degradation of ε-PL [77].

Ideally, injectable biomaterials for bone regeneration should degrade at a rate that matches the growth rate of new bone tissue to ensure proper structural integrity throughout the healing process. Optimally, the biomaterial should fully resorb over several months to years [81].

Degradation of the nanocomposite hydrogels is expected to be accompanied by ion release from the Sr-HAp. Biomaterials, which can ensure the long-term (months to years) local supply of the Sr^{2+} ions, have been proposed to be suitable for patients with osteoporotic fractures or bone defects [82]. Since we intended the nanocomposite hydrogels to be carriers of Sr^{2+} ions, the cumulative ion release under physiological conditions was analyzed for 3 months (Fig. 5(b,c)). Generally, the higher the mass ratio of the Sr-HAp, the higher the amount of released ions. However, the amount of released ions from the Sr-HAp paste was lower. The amount of the released ions from the Sr-HAp/ε-PL-HA hydrogels significantly increased due to the burst release of the Sr^{2+} and Ca^{2+} ions in the first few days. It is well known that the dissolution of HAp is inversely related to pH. The dissolution of nanocrystalline HAp at pH 5 (pH of the ε-PL-HA hydrogels) is accompanied by a rapid initial increase in the Ca^{2+} and PO_4^{3-} ions concentrations, followed by a gradual decrease as the pH increases [83]. Thus, the significant burst release from the nanocomposite hydrogels could be related to their acidic nature. Namely, partial dissolution of Sr-HAp particles may have occurred in the hydrogel matrix, creating free ions. The free ions were most likely released during the first days, thus causing burst release. The burst release can cause an adverse effect as the high local concentration of the Sr^{2+} ions can result in cytotoxicity [82].

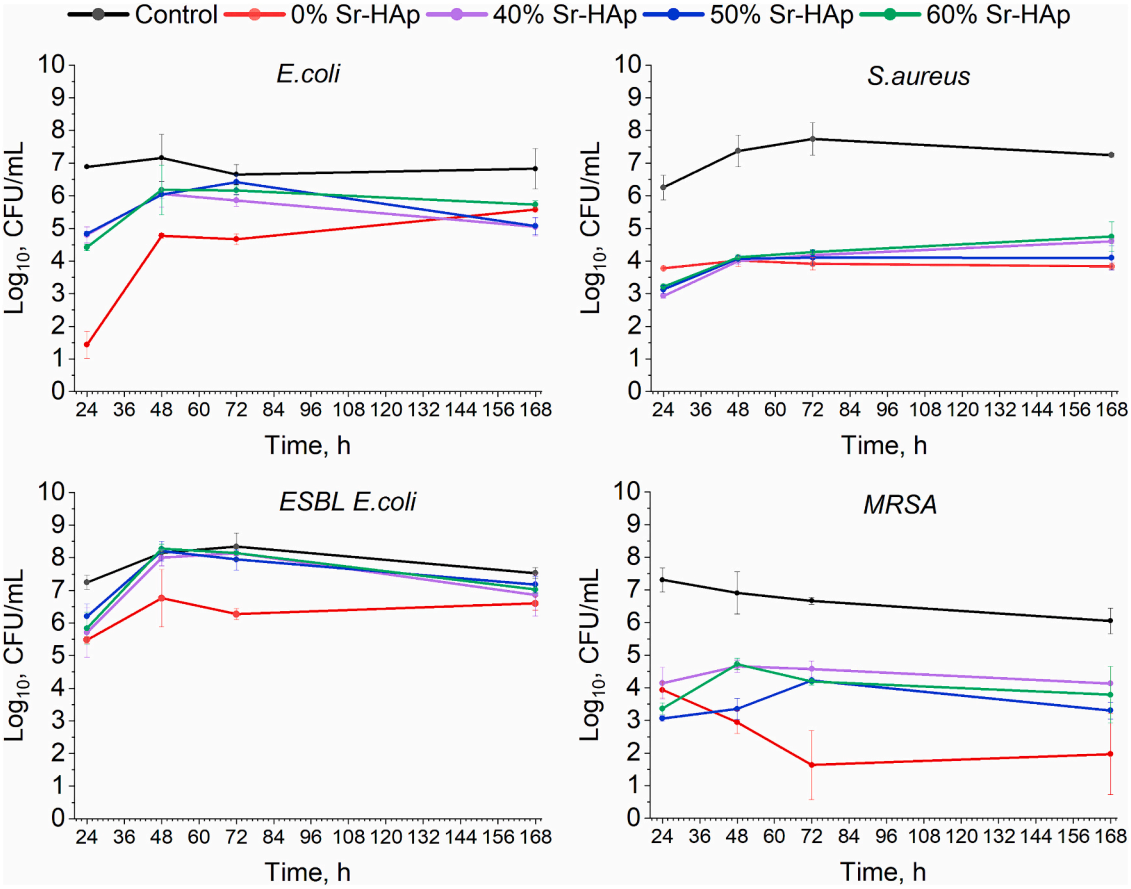

Fig. 6. Antibacterial activity of the as-prepared Sr-HAp-loaded ε-PL-HA nanocomposite hydrogels on *E. coli*, *S. aureus, ESBL E. coli,* and *MRSA* bacteria strains (n = 3) (COLOR).

However, the concentration of Sr^{2+} ions released from the nanocomposite hydrogels does not exceed 20–30 μM. Our earlier study suggests that up to 40 μM of Sr^{2+} ions in the cell culture is beneficial for the proliferation of MG-63 osteoblasts [41]. In addition, the simultaneous release of Ca^{2+} ions in relatively high concentrations should also be considered. Up to 200 μM of Ca^{2+} ions were burst-released in the first days. According to the literature, elevated Ca^{2+} ions concentration (up to 900 μM) enhances the bone regeneration effects of Sr^{2+} ions [84]. The burst release was followed by slow and continuous release of Sr^{2+} and Ca^{2+} ions over 3 months.

3.6. Antibacterial properties

The ε-PL with a cationic surface because of its positively charged amino acid residues is expected to act as an antibacterial component in the Sr-HAp/ε-PL-HA nanocomposite hydrogels. Thus, the antibacterial activity of the as-prepared Sr-HAp/ε-PL-HA hydrogels against *E. coli*, *ESBL E. coli* (Gram-negative) and *S. aureus*, MRSA (Gram-positive) was assessed using the standard plate counting microdilution method (Fig. 6).

To evaluate the long-term antibacterial activity, the bacteria were subjected to direct contact with the hydrogels, and experimental time points were 24 h, 48 h, 72 h, and 168 h. At all experimental time points, it was observed that the nanocomposite hydrogels induced statistically significant (statistical analysis is shown in Fig. S8) reduction in the number of bacterial colonies of Gram-positive reference and clinically isolated antibiotic-resistant *S. aureus* strains. All experimental series showed fast-acting and long-term antibacterial activity against both *S. aureus* strains. In the case of Gram-negative *E. coli* and ESBL *E. coli* strains, the hydrogels showed a significant reduction in bacterial colonies only in a fast-acting perspective, *i.e.*, after 24 h. Structural features of Gram-negative bacteria cell walls could explain this tendency. The presence and polarity of the outer membrane of Gram-negative bacteria prevent the achievement of cationic on the bacterial membrane surface, resulting in reduced antibacterial action [85]. Furthermore, the presence of the inorganic phase, namely, the Sr-HAp, might compromise the antibacterial profile of the composite hydrogels [86] by affecting the release of the antibacterial component or creating a physical barrier in the matrix. Statistically significant differences were found between the 0 % Sr-HAp hydrogels and Sr-HAp-loaded nanocomposite hydrogels at different experimental stages. For example, in the case of *E. coli* at the 24 h point, the 0 % Sr-HAp series showed significantly higher inhibition than other compositions. As for 48 h and 72 h, 0 % Sr-HAp hydrogels were the only ones to maintain antibacterial activity against *E. coli*. This difference might arise because the Sr-HAp increases physical entanglements in the polypeptide network and slows the release of antibacterial ε-PL. As mentioned above, such deacceleration of ε-PL release leads to a decreased concentration of ε-PL molecules on the bacterial surface below its' antibacterial effect. No significant differences were found between Sr-HAp/ε-PL-HA nanocomposite hydrogels with different Sr-HAp mass ratios, suggesting that the Sr-HAp does not have an impact on the antibacterial activity of the ε-PL-HA hydrogels.

Overall, the Sr-HAp/ε-PL-HA nanocomposite hydrogels possess fast-acting and long-term antibacterial activity against Gram-positive bacteria and can inhibit Gram-negative bacteria in a fast-acting perspective. Although the antibacterial activity provided by the ε-PL is desirable, they might be hampered by the risk of cytotoxicity. To evaluate whether the addition of the Sr-HAp improves the biocompatibility of the ε-PL-HA hydrogels, *in vitro* cell tests were performed.

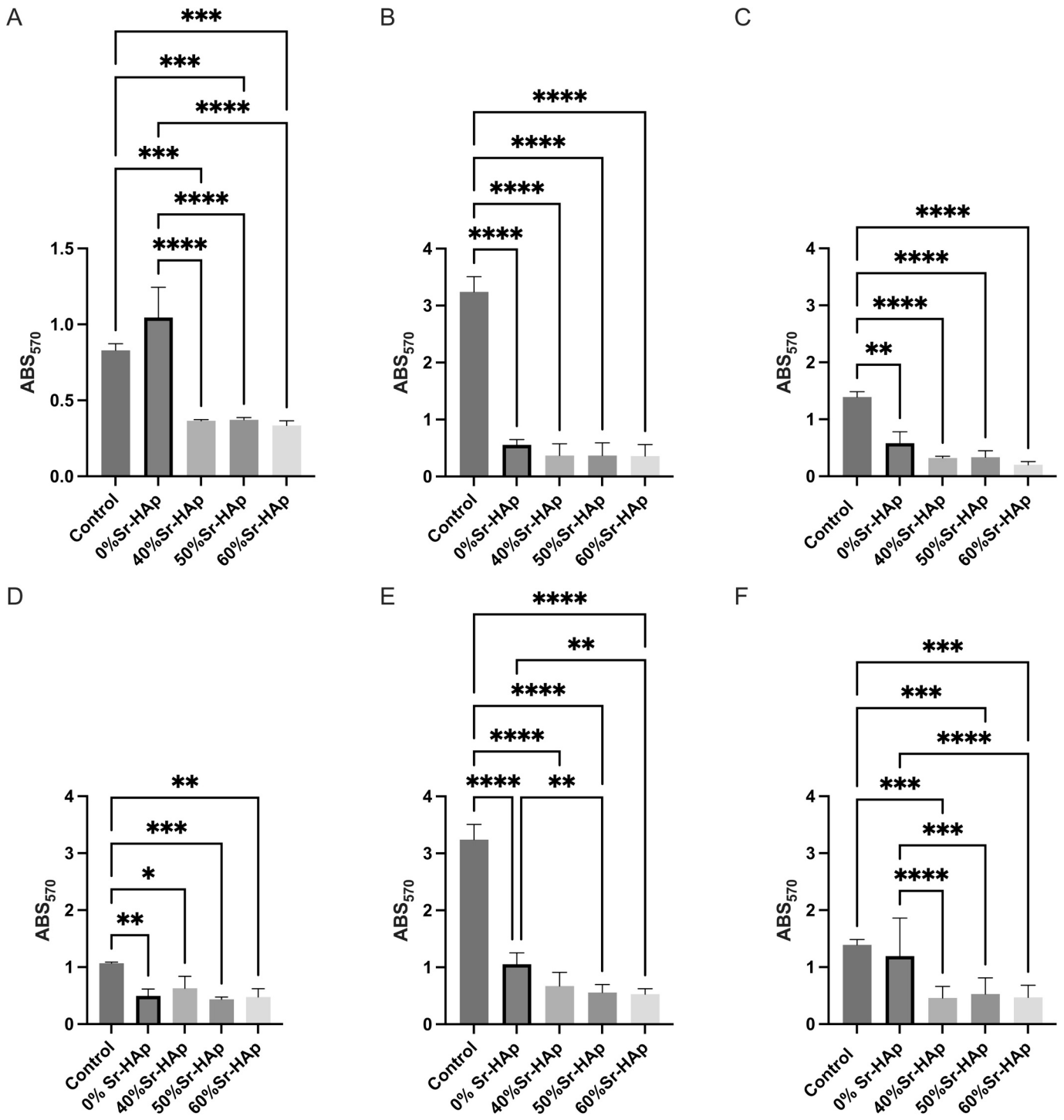

Fig. 7. Effect of the Sr-HAp-loaded ε-PL-HA nanocomposite hydrogels on the proliferation of MG-63 osteoblasts in the hydrogels (A, B, C) and on the cultivation plate surface surrounding the hydrogel (D, E, F) after 2 (A, D), 5 (B, E), and 7 (C, F) days of cultivation, control – cells grown in standard cultivation conditions (ANOVA: * for $p < 0.05$, ** - for $p < 0.01$, *** - for $p < 0.001$ **** for $p < 0.0001$, $n = 3$).

3.7. *In vitro biocompatibility*

3.7.1. *Proliferation of osteoblasts and pre-osteoblasts*

The proliferation of MG-63 osteoblasts (Fig. 7) and MC3T3-E1 pre-osteoblast (Fig. 8) was evaluated on days 2, 5, and 7. It was observed that some of the cells seeded onto the hydrogels tend to migrate, attach, and proliferate on the cultivation plate surface surrounding the hydrogels. The samples and the corresponding plate wells were assayed separately to assess the proportion of cells growing around the hydrogel *versus* those in the hydrogel samples.

The proliferation of MG-63 cells was lower in the hydrogels (Fig. 7 (A-C)) than on the cultivation plate (Fig. 7(D—F)), especially on days 5 and 7. This could be explained by dissolution of the hydrogels in the culture medium. As the hydrogel dissolves, the released components are evenly distributed in the culture media and over the surface of the cultivation plate. Thus, cell migration and proliferation outside the hydrogels could be promoted.

In the case of 0 % Sr-HAp, the highest MG-63 cell proliferation in the

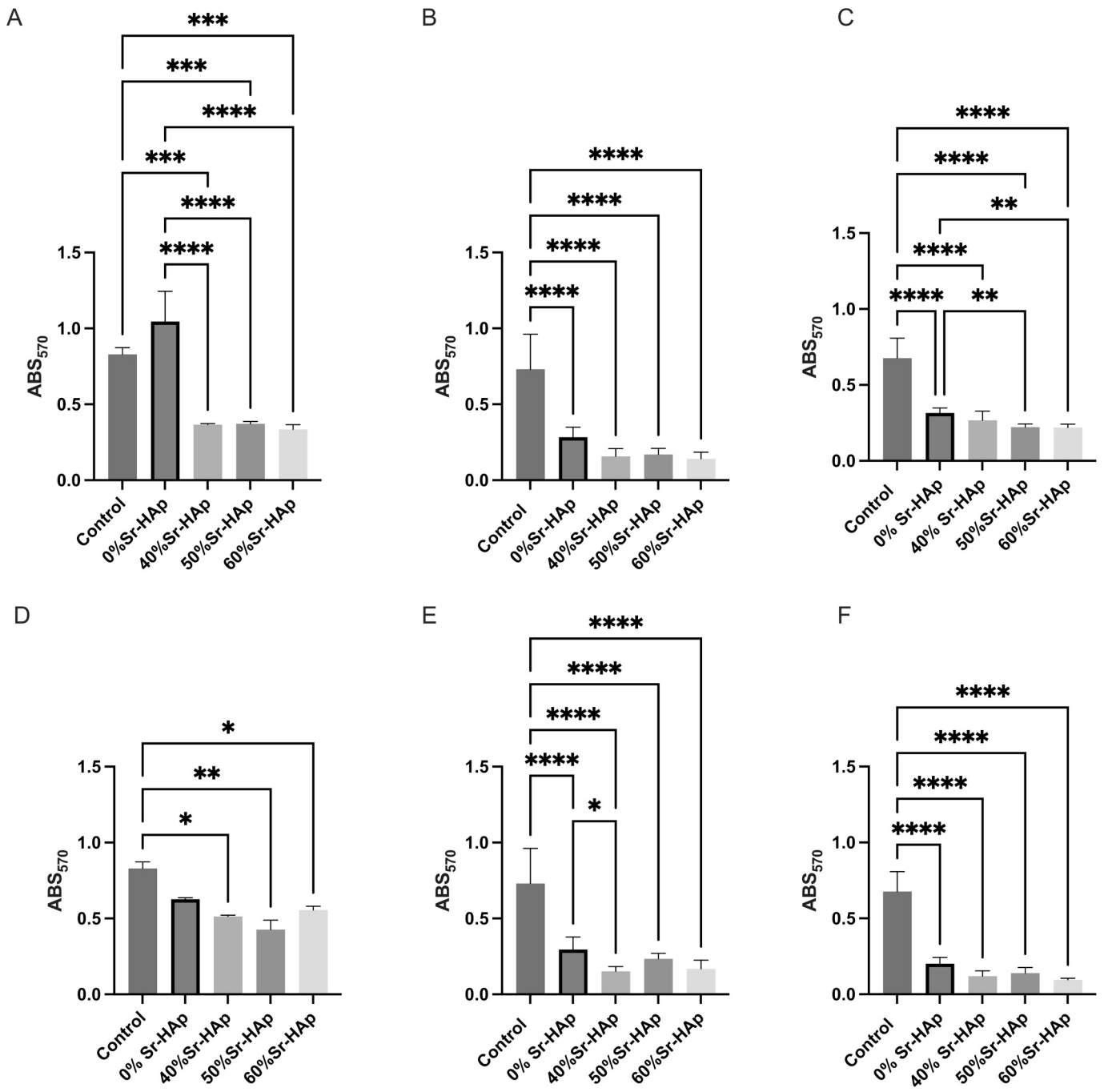

Fig. 8. Effect of the Sr-HAp-loaded ε-PL-HA nanocomposite hydrogels on the proliferation of the MC3T3-E1 pre-osteoblasts in the hydrogels (A, B, C) and on the cultivation plate surface surrounding the hydrogel (D, E, F) after 2 (A, D), 5 (B, E), and 7 (C, F) days of cultivation, control – cells grown in standard cultivation conditions (ANOVA: * for $p < 0.05$, ** - for $p < 0.01$, *** - for $p < 0.001$, **** for $p < 0.0001$, $n = 3$).

hydrogels and on the cultivation plate surface was observed. At 2 days after seeding, cell proliferation in 0 % Sr-HAp even slightly exceeded that of the control cells. Moreover, the superiority of 0 % Sr-HAp compared to the hydrogels containing Sr-HAp increased with incubation time. Moreover, no significant differences were observed among the hydrogels with various mass ratios of the Sr-HAp, and the proliferation of the MG-63 cells in the hydrogels decreased on day 5 and day 7. A similar tendency was observed on the cultivation plate surface. This is contrary to information in the literature suggesting that adding HAp to the polymer composites [87] and the presence of Sr in the biomaterials [88,89] leads to higher osteogenic activity, including the proliferation of the osteoblasts. This could be due to the influence of the microstructure of hydrogels. The 0 % Sr-HAp hydrogels are significantly more porous than the nanocomposite hydrogels (Fig. 4(c,e)) and, thus, more favorable to cell migration inside the samples [72]. At the same time, differences in the proliferation of the MG-63 cells on the cultivation plate could be related to the differences in degradation (*i.e.*, the released components (ions, polymers)) of the hydrogels. Up to 0.250 mM of Ca^{2+} and 0.025 mM Sr^{2+} ions were released from all the Sr-HAp/ε-PL-HA hydrogels in 7 days (Fig. 5). Regarding released Ca^{2+} ion concentration, it has been suggested that 2–4 mM is optimal for the survival and proliferation of osteoblasts, 6–8 mM favor osteoblast differentiation and matrix mineralization, and concentrations above 10 mM are considered cytotoxic [90]. According to the literature, the Sr^{2+} ions therapeutic

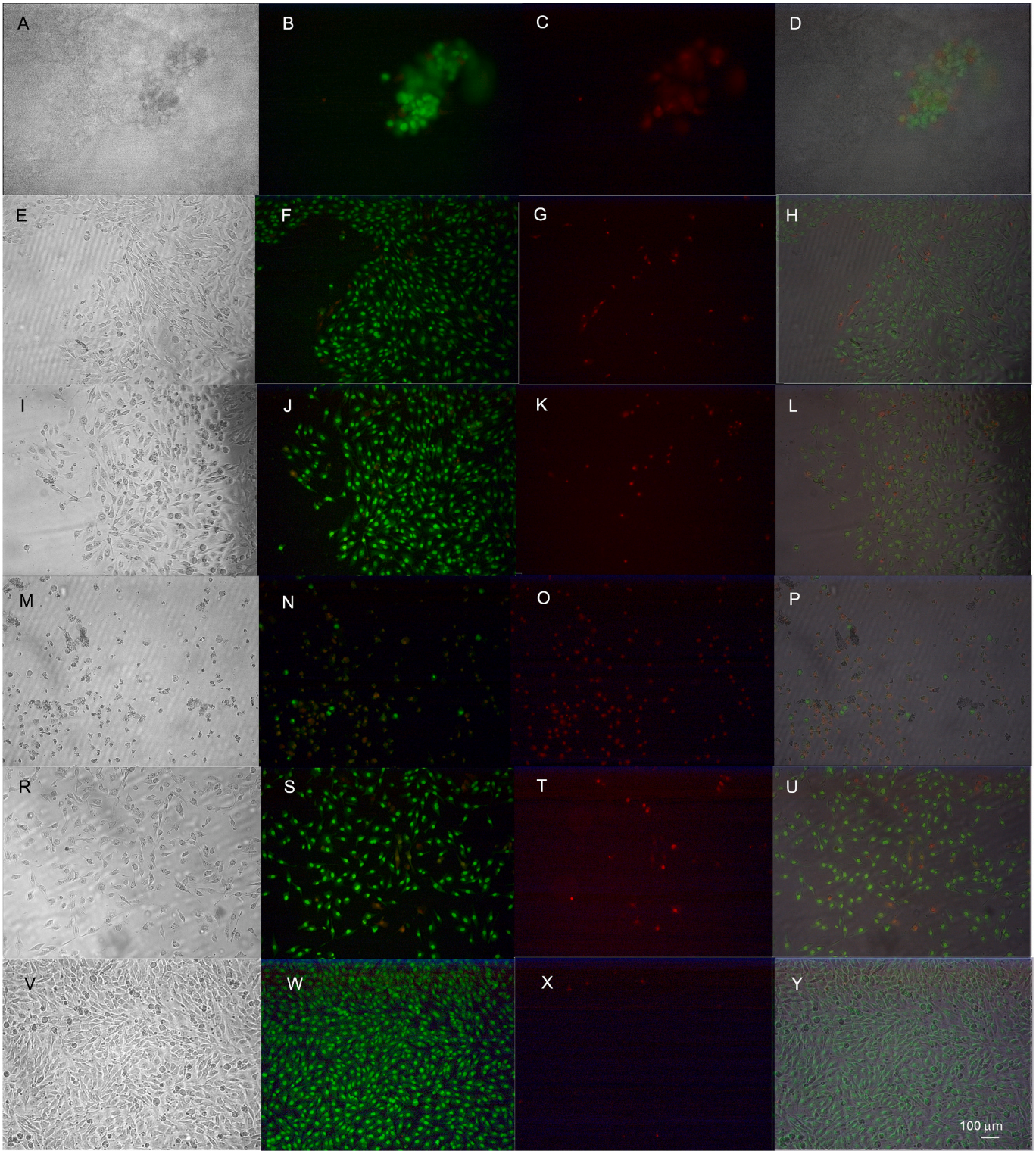

Fig. 9. Live/dead staining of MG-63 osteoblasts after 5 days of cultivation. MG-63 osteoblasts A - D – in the 0 % Sr-HAp hydrogel, and on the cultivation plate surface surrounding E - H – the 0 % Sr-HAp, I - L – 40 % Sr-HAp, M - P –50 % Sr-HAp, R - U - 60 % Sr-HAp hydrogels, *V*—Y – control cells grown on the surface (A, E, I, M, R, V – brightfield; B, F, J, N, S, W– SYTO 9 (green); C, G, K, O, T, X – propidium iodide (red); D, H, L, P, U, Y – merged images; the scale bar represents 100 µm).

level is 2–45 ppm (0.02–0.52 mM) [91]. Thus, the concentrations of Ca^{2+} and Sr^{2+} ions released in 7 days can be considered safe. However, the Sr-HAp/ε-PL-HA hydrogels are more susceptible to enzymatic degradation than the ε-PL-HA hydrogels. This could have resulted in a higher initial release of organic substances from the polymers upon incubation in the cell culture media, affecting cell behavior.

In the case of the MC3T3-E1 cells, the proliferation was slightly higher in the hydrogels (Fig. 8(A-C)) than on the cultivation plate surface surrounding the hydrogels (Fig. 8(D—F)). MC3T3-E1 proliferation in the hydrogels and on the cultivation plate surface decreased over time. This indicates the different sensitivity of the MG-63 and MC3T3-E1 cell lines to the components of the hydrogels. It has been reported that

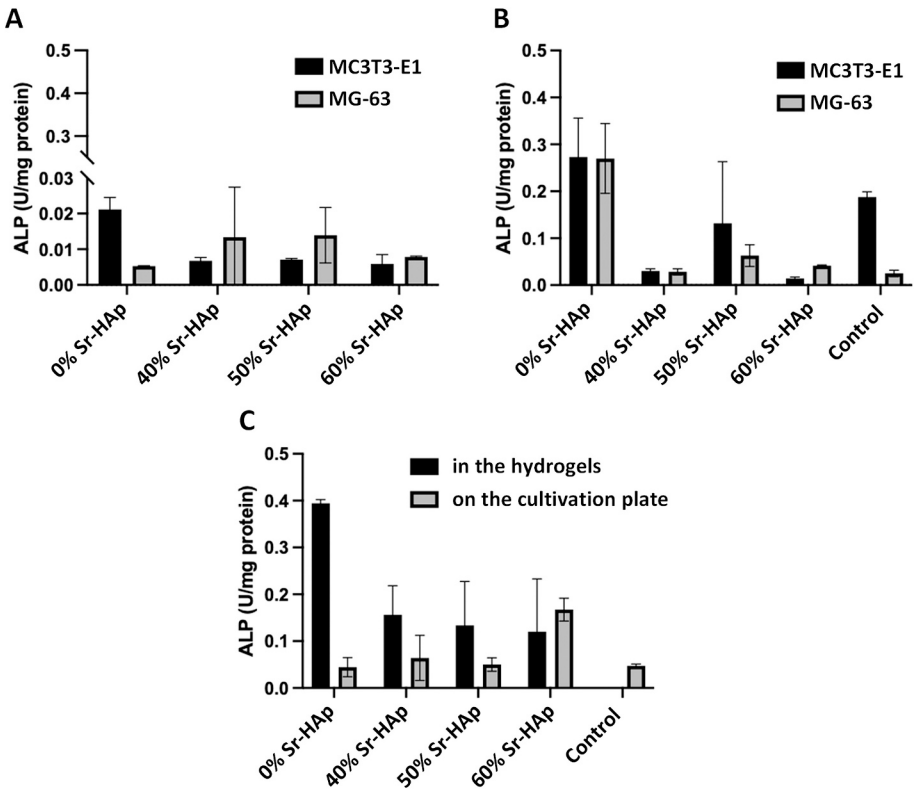

Fig. 10. The ALP activity in the lysates from the MC3T3-E1 and the MG-63 cells (A) grown in the hydrogels, (B) on the cultivation plate in the presence of the hydrogels for 5 days, and (C) in the lysates from the MG-63 cells grown in the hydrogels and on the cultivation plate in the presence of the hydrogels for 7 days (n = 3).

low concentrations (up to 0.18 mM) of Sr^{2+} ions have MC3T3-E1 proliferation and osteogenesis-stimulating activity, while high concentrations (above 24 mM) have been shown to reduce cell viability [92,93]. Like MG-63 osteoblasts, MC3T3-E1 pre-osteoblasts showed higher proliferation in the 0 % Sr-HAp hydrogel, with the most pronounced differences observed on day 2.

To further characterize the growth and morphology of the cells, live/dead staining was performed after 5- and 7-day cultivation of MG-63 and MC3T3-E1 cells on the hydrogels. Detecting live cells using live/dead dyes proved challenging due to the hydrogel structure. Single cells or small clusters were found in all hydrogels, but cell densities were generally low, with both live and dead cells present (Fig. S9 – Fig. S12). MG-63 cells grew more noticeably outside the hydrogel, *i.e.*, on the cultivation plate surface surrounding the hydrogels, which aligns with the MTT assay results. Growth on the cultivation plate surface indicates that cells prefer to grow on standard cell cultivation plastic compared to the nanocomposite hydrogels. Still, the presence of hydrogels and the potential leakage of components from them did not significantly affect cell viability and morphology. More viable cells were observed in the 0 % Sr-HAp hydrogels compared to the Sr-HAp-loaded nanocomposite hydrogels. Cells predominantly were localized at the edges of the material (Fig. 9, Fig. S9(A-H), Fig. S10(A-C), Fig. S11(A-C)). Interestingly, less viable MG-63 cells were observed in the presence of the 50 % Sr-HAp samples compared to other nanocomposite hydrogels. Higher density and viability were observed in control cells. However, cell density and viability after 5 days and 7 days also increased in the presence of hydrogels, indicating that the potential cytotoxic effect is weak and during continuous cultivation, cells continue to grow and proliferate (Fig. S9(M-P), Fig. S10(M-P)). All hydrogels supported live MC3T3-E1 cells after 5 and 7 days of culture. Cell numbers observed in the hydrogels were low; however, normal cell morphology was observed (Figs. S10-S11).

In general, both cell lines showed viability in the hydrogels and on the cultivation plate surface surrounding the hydrogels, indicating that the hydrogels are not cytotoxic. However, the proliferation rates varied depending on the cell line. Although the Sr-HAp loading in the ε-PL-HA nanocomposite hydrogels did not show proliferation-stimulating activity, it should be noted that a substantial part of the Sr-HAp is embedded in the hydrogel matrix as observed from the SEM analysis (Fig. 4(f)) and, thus, not in direct contact with the cells upon initial stages of incubation. Therefore, the significant effect from the Sr-HAp would be observed upon the dissolution of the nanocomposite hydrogels in the cell culture medium.

3.7.2. *Alkaline phosphatase activity*

ALP activity is generally used as an early marker for osteodifferentiation *in vitro*. Thus, the ALP activity in both cell lines was measured in the lysates from cells grown in the hydrogels and on the cultivation plate in the presence of the hydrogels (Fig. 10).

Regarding the cells grown in the hydrogels for 5 days, the highest ALP activity of the MC3T3-E1 was observed in the case of the 0 % Sr-HAp hydrogels (Fig. 10(A)). In turn, the ALP activity of the MC3T3-E1 cells grown in the Sr-HAp/ε-PL-HA hydrogels did not differ significantly. Meanwhile, the ALP activity of the MG-63 cells grown in the hydrogels for 5 days was equal for all hydrogel compositions. However, after 7 days of cultivation, the ALP activity of the MG-63 cells grown in the hydrogels increased, the highest being in the case of the 0 % Sr-HAp (Fig. 10(C)). In general, the ALP activity of the lysates from cells grown in the hydrogels was lower than for cells grown on the cultivation plate (Fig. 10(B)). According to the literature, ALP expression can be downregulated when grown in 3D cultures compared to plastic-surface cultivation [94]. Also, for the cells grown on the cultivation plate in the presence of hydrogels for 5 days, the highest ALP activity for both cell lines was observed in the case of 0 % Sr-HAp (Fig. 10(B)). Moreover, for the MC3T3-E1, the ALP activity in the case of 0 % Sr-HAp was higher than those grown on the cultivation plate without the hydrogels

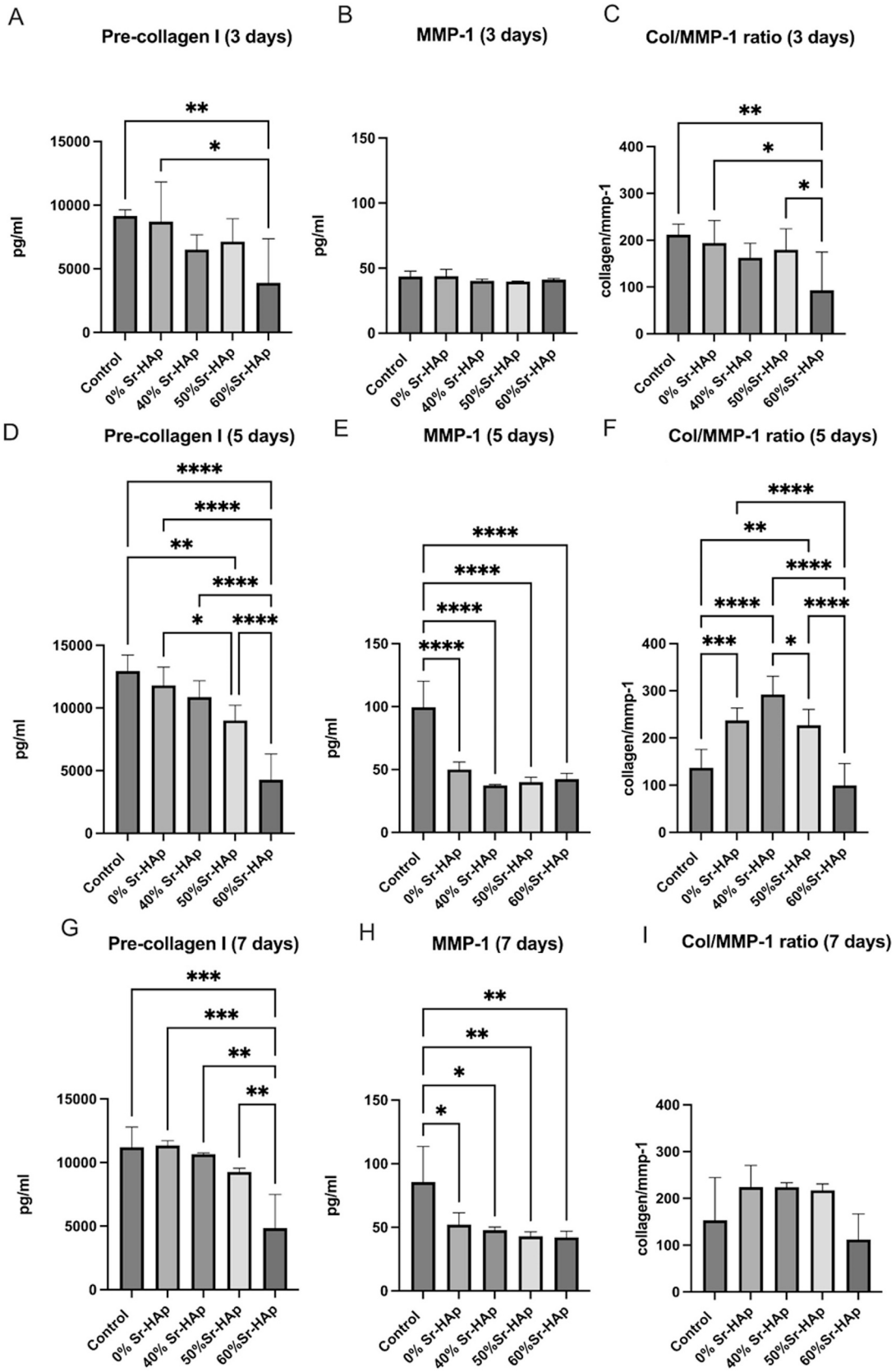

Fig. 11. Secretion of pre-collagen I (A, D, G) and MMP-1 (B, E, H) and ratio between pre-collagen I and MMP-1 (Col/MMP-1 ratio, C, F, I) after 3, 5, and 7 days of MG-63 cultivation on the Sr-HAp-loaded nanocomposite hydrogels (ANOVA: * for $p < 0.05$; ** $p < 0.01$, for *** - for $p < 0.001$, **** for $p < 0.0001$, $n = 3$).

(control), indicating the stimulating activity of the 0 % Sr-HAp. In the case of MG-63, the ALP activity higher than the control was in the lysates of the cells grown in the presence of 0 % Sr-HAp, 50 % Sr-HAp, and 60 % Sr-HAp hydrogels. These observations correlate with cell proliferation assays (Fig. 7 and Fig. 8). Upregulation of ALP production is more pronounced at higher cell densities [95,96]. Thus, the lower proliferation of MG-63 and MC3T3-E1 cells in the Sr-HAp/ε-PL-HA hydrogels compared to the 0 % Sr-HAp could explain the observed tendencies of ALP activities. Interestingly, the lysates of the MG-63 osteoblasts grown for 7 days on the cultivation plate in the presence of the 0 % Sr-HAp hydrogels showed significantly lower ALP activity than after 5 days of cultivation (Fig. 10(C)). A similar effect was observed in cell studies of Sr-incorporated HAp bioceramics using bone marrow mesenchymal cells. Namely, the ALP activity after 7 days of cultivation increased compared to 4-day cultivation [97]. In addition, *Tsai* et al. observed that the MG-63 ALP activity was the highest after 3 days of cultivation in the presence of Sr-substituted HAp nanofibrous matrix and decreased during prolonged cultivation [88]. Also, changes in ALP activity in the lysates from cells grown on the cultivation plate could be explained by the release of Sr^{2+} and other hydrogel components. The studies found in the literature show that ALP activity highly depends on the concentration of Sr in the tested materials and the release of Sr^{2+} ions in the culture medium. Generally, it has been reported before that Sr^{2+} ions released from various biomaterials stimulate osteogenesis [98,99]. Even low Sr ratios in composite materials are reported to positively affect ALP activity in MC3T3-E1 cells; however, increasing Sr content leads to lower ALP activity [99]. *Xie* et al. reported that stimulation of ALP activity by Sr^{2+} ions released from biomaterials depends on Ca^{2+} concentrations [84].

3.7.3. Secretion of pre-collagen and MMP-1

The organic part of bone ECM is composed mainly of collagen type I, primarily synthesized by osteoblasts. Collagen acts as the scaffold for bone cells, promotes bone formation, and provides mechanical support and bone strength [100]. ECM is dynamic, and it continuously undergoes remodeling mediated by enzymes MMPs. MMPs are involved in bone tissue regeneration and repair. Regulation of matrix formation and remodeling is crucial for tissue homeostasis [101]. Increased levels of MMPs are characteristic of inflammatory bone diseases and infections. Elevated levels of MMP-1 and mutations in corresponding genes lead to increased degradation of collagen I and are associated with the development of osteoporosis [102].

In this study, the pre-collagen I and MMP-1 levels secreted by MG-63 cells grown in the Sr-HAp-loaded nanocomposite hydrogels for 3, 5, and 7 days were measured (Fig. 11).

At all cultivation times, the cells grown in the 0 % Sr-HAp hydrogels produced pre-collagen I at a similar level to the control. On days 5 and 7, the pre-collagen I level decreased with increasing the mass ratios of Sr-HAp in the hydrogels. The most pronounced increase in the pre-collagen I was observed for the 40 % Sr-HAp hydrogels. From day 3 to day 7, the pre-collagen I concentration in the presence of 40 % Sr-HAp hydrogels increased by an average of 4143 pg/mL, while in the control - an average of 2056 pg/mL. No correlation between collagen production and cell proliferation was observed. This allows us to assert that even if the nanocomposite hydrogels do not stimulate cell proliferation, they promote pre-collagen I synthesis in osteoblasts and ECM production.

After 3 days of cultivation, the MMP-1 secretion for all hydrogels was similar to the control level. Still, after 5 and 7 days, the MMP-1 secretion of the cells in the presence of 0 % Sr-HAp hydrogels increased.

The pre-collagen I to MMP-1 (Col/MMP-1) ratios were calculated to evaluate if the hydrogels in the cultivation media promote collagen production or degradation. Higher Col/MMP-1 ratios indicate a predominance of collagen synthesis over degradation. After 5 and 7 days of cultivation, the 0 % Sr-HAp, 40 % Sr-HAp, and 50 % Sr-HAp hydrogels provided conditions where collagen synthesis exceeds degradation compared to the control. The highest Col/MMP- ratios were observed on day 5. In the case of 60 % Sr-HAp, the Col/MMP-1 ratios were lower than the control's, indicating lower ECM synthesis-promoting activity.

A study with murine osteoblasts showed that collagen matrix is required for cell differentiation and increased ALP expression [103]. This was partly observed in our research. The highest pre-collagen I concentrations were achieved after 7 days of cultivation in the 0 % Sr-HAp hydrogels. The lysates from cells grown in the 0 % Sr-HAp hydrogels also had the highest ALP activity after the same cultivation period. High average ALP activity was obtained in the lysate of MG-63 cells grown for 5 days in the 40 % Sr-HAp hydrogels, and the highest Col/MMP-1 ratio was calculated, indicating a correlation between collagen production and ALP activity. A correlation between collagen production and ALP activity was not observed for the rest of the nanocomposite hydrogels.

4. Conclusions

The Sr-hydroxyapatite loaded ε-polylysine-hyaluronic acid hydrogels that can be manually injected, set *in situ*, and offer structural support and temporary scaffold for bone defect filling were successfully prepared. The physical properties, including injectability, syneresis, swelling, gel fraction, and degradation kinetics, can be optimized by changing the mass ratio of the Sr-HAp. The nanocomposite hydrogels slowly release Sr^{2+} and Ca^{2+} ions at therapeutic bone regeneration concentrations. Furthermore, they show outstanding antibacterial activity and collagen synthesis-promoting activity.

CRediT authorship contribution statement

A. Rubina: Writing – original draft, Visualization, Validation, Methodology, Investigation, Formal analysis, Data curation, Conceptualization. **A. Sceglovs:** Writing – review & editing, Writing – original draft, Visualization, Investigation, Formal analysis, Conceptualization. **A. Ramata-Stunda:** Writing – original draft, Visualization, Validation, Methodology, Investigation, Formal analysis. **I. Pugajeva:** Writing – review & editing, Visualization, Methodology, Investigation. **I. Skadins:** Writing – review & editing, Methodology, Investigation. **A.R. Boyd:** Writing – review & editing, Methodology, Investigation. **A. Tumilovica:** Visualization, Methodology, Investigation. **L. Stipniece:** Writing – review & editing, Writing – original draft, Visualization, Validation, Supervision, Methodology, Conceptualization. **K. Salma-Ancane:** Writing – review & editing, Writing – original draft, Validation, Supervision, Resources, Methodology, Funding acquisition, Conceptualization.

Declaration of competing interest

The authors declare that they have no known competing financial interests or personal relationships that could have appeared to influence the work reported in this paper.

Data availability

Data will be made available on request.

Acknowledgments

The authors acknowledge financial support from the European Union's Horizon 2020 research and innovation programme under the grant agreement No. 857287.

The authors thank Anastasija Borisova (Institute of Food Safety, Animal Health and Environment "BIOR") for her excellent help in ICP-MS analysis.

Appendix A. Supplementary data

Supplementary data to this article can be found online at https://doi.

org/10.1016/j.ijbiomac.2024.135703.

References

[1] T. Winkler, F.A. Sass, G.N. Duda, K. Schmidt-Bleek, A review of biomaterials in bone defect healing, remaining shortcomings and future opportunities for bone tissue engineering: the unsolved challenge, Bone Joint Res. 7 (2018) (2018) 232–243, https://doi.org/10.1302/2046-3758.73.BJR-2017-0270.R1.

[2] Osteoporosis: A Global Health Crisis - NBI. https://www.nbihealth.com/osteoporosis-global-health-crisis/, 2023 (Accessed 24 January, 2023).

[3] E.H. Schemitsch, Size matters: defining critical in bone defect size!, J. Orthop. Trauma 31 (2017) S20–S22, https://doi.org/10.1097/bot.0000000000000978.

[4] E. Hernlund, A. Svedbom, M. Ivergård, J. Compston, C. Cooper, J. Stenmark, E. V. McCloskey, B. Jönsson, J.A. Kanis, Osteoporosis in the European Union: medical management, epidemiology and economic burden, Arch. Osteoporos. 8 (2013), https://doi.org/10.1007/s11657-013-0136-1.

[5] M. Fontcuberta-Rigo, M. Nakamura, P. Puigbò, Phylobone: a comprehensive database of bone extracellular matrix proteins in human and model organisms, Bone Res. 11 (2023), https://doi.org/10.1038/s41413-023-00281-w.

[6] P.J. Meeder, C. Eggers, The history of autogenous bone grafting, Injury 25 (1994) A2–A3, https://doi.org/10.1016/0020-1383(94)90254-2.

[7] J. Adhikari, P. Saha, A. Sinha, Surface modification of metallic bone implants-polymer and polymer-assisted coating for bone in-growth, in: P. Balakrishnan, S. M.S. Sabu Thomas (Eds.), Fundamental Biomaterials: Metals, Woodhead Publishing, 2018, pp. 299–321, https://doi.org/10.1016/B978-0-08-102205-4.00014-3.

[8] G. Kaur, V. Kumar, F. Baino, J.C Mauro, G. Pickrell, I. Evans, O. Bretcanu, Mechanical properties of bioactive glasses, ceramics, glass-ceramics and composites: state-of-the-art review and future challenges, Mater. Sci. Eng. C Mater. Biol. Appl. 104 (2019) 109895. doi:https://doi.org/10.1016/j.msec.2019.109895.

[9] J. Zhang, W. Liu, V. Schnitzler, F. Tancret, J.M. Bouler, Calcium phosphate cements for bone substitution: chemistry, handling and mechanical properties, Acta Biomater. 10 (2014) 1035–1049, https://doi.org/10.1016/j.msec.2019.109895.

[10] G. Tozzi, A. De Mori, A. Oliveira, M. Roldo, Composite hydrogels for bone regeneration, Materials (Basel) 9 (2016), https://doi.org/10.3390/ma9040267.

[11] X. Ren, X. Chen, Z. Geng, J. Su, Bone-targeted biomaterials: strategies and applications, Chem. Eng. J. 446 (2022) 137133, https://doi.org/10.1016/j.cej.2022.137133.

[12] R. Menezes, R. Vincent, L. Osorno, P. Hu, T.L. Arinzeh, Biomaterials and tissue engineering approaches using glycosaminoglycans for tissue repair: lessons learned from the native extracellular matrix, Acta Biomater. 163 (2023) 210–227, https://doi.org/10.1016/j.actbio.2022.09.064.

[13] Y.M. Coulson-Thomas, V.J. Coulson-Thomas, A.L. Norton, T.F. Gesteira, R. P. Cavalheiro, M.C.Z. Meneghetti, J.R. Martins, R.A. Dixon, H.B. Nader, The identification of proteoglycans and glycosaminoglycans in archaeological human bones and teeth, PloS One 10 (2015) e0131105, https://doi.org/10.1371/journal.pone.0131105.

[14] J.M. Anderson, J.L. Patterson, J.B. Vines, A. Javed, S.R. Gilbert, H.W. Jun, Biphasic peptide amphiphile nanomatrix embedded with hydroxyapatite nanoparticles for stimulated osteoinductive response, ACS Nano 5 (2011) 9463–9479, https://doi.org/10.1021/nn203247m.

[15] K. Phogat, S.B. Ghosh, S. Bandyopadhyay-Ghosh, Recent advances on injectable nanocomposite hydrogels towards bone tissue rehabilitation, J. Appl. Polym. Sci. 140 (2023) e53362, https://doi.org/10.1002/app.53362.

[16] L. Huang, Y.Y. Cheng, P.L. Koo, K.M. Lee, L. Qin, J.C.Y. Cheng, S.M. Kumta, The effect of hyaluronan on osteoblast proliferation and differentiation in rat calvarial-derived cell cultures, J. Biomed. Mater. Res. 66A (2003) 880–884, https://doi.org/10.1002/jbm.a.10535.

[17] C.B. Highley, G.D. Prestwich, J.A. Burdick, Recent advances in hyaluronic acid hydrogels for biomedical applications, Curr. Opin. Biotechnol. 40 (2016) 35–40, https://doi.org/10.1016/j.matpr.2022.12.208.

[18] P. Ghandforoushan, M. Alehosseini, N. Golafshan, M. Castilho, A. Dolatshahi-Pirouz, J. Hanaee, S. Davaran, G. Orive, Injectable hydrogels for cartilage and bone tissue regeneration: a review, Int. J. Biol. Macromol. 246 (2023) 125674, https://doi.org/10.1016/j.ijbiomac.2023.125674.

[19] M. Liu, X. Zeng, C. Ma, Y. Huan, Z. Ali, X. Mou, S. Li, Y. Deng, N. He, Injectable hydrogels for cartilage and bone tissue engineering, Bone Res. 5 (2017) 17014, https://doi.org/10.1038/boneres.2017.14.

[20] G. Kogan, L. Šoltés, R. Stern, P. Gemeiner, Hyaluronic acid: a natural biopolymer with a broad range of biomedical and industrial applications, Biotechnol. Lett. 29 (2007) 17–25, https://doi.org/10.1007/s10529-006-9219-z.

[21] S. Li, M. Pei, T. Wan, H. Yang, S. Gu, Y. Tao, X. Liu, Y. Zhou, W. Xu, P. Xiao, Self-healing hyaluronic acid hydrogels based on dynamic Schiff base linkages as biomaterials, Carbohydr. Polym. 250 (2020) 116922, https://doi.org/10.1016/j.carbpol.2020.116922.

[22] X. Yu, X. Tang, S.V. Gohil, C.T. Laurencin, Biomaterials for bone regenerative engineering, Adv. Healthc. Mater. 4 (2015) 1268–1285, https://doi.org/10.1002/adhm.201400760.

[23] H. Zhang, S. Wu, W. Chen, Y. Hu, Z. Geng, J. Su, Bone/cartilage targeted hydrogel: strategies and applications, Bioact. Mater. 23 (2022) 156–169, https://doi.org/10.1016/j.bioactmat.2022.10.028.

[24] L. Wang, C. Zhang, J. Zhang, Z. Rao, X. Xu, Z. Mao, X. Chen, Epsilon-poly-L-lysine: recent advances in biomanufacturing and applications, Front. Bioeng. Biotechnol. 9 (2021) 748976, https://doi.org/10.3389/fbioe.2021.748976.

[25] K. Salma-Ancane, A. Sceglovs, E. Tracuma, J.K. Wychowaniec, K. Aunina, A. Ramata-Stunda, V. Nikolajeva, D. Loca, Effect of crosslinking strategy on the biological, antibacterial and physicochemical performance of hyaluronic acid and ε-polylysine based hydrogels, Int. J. Biol. Macromol. 208 (2022) 995–1008, https://doi.org/10.1016/j.ijbiomac.2022.03.207.

[26] A. Sceglovs, J.K. Wychowaniec, I. Skadins, A. Reinis, C.J.C. Edwards-Gayle, M. D'Este, K. Salma-Ancane, Effect of steam sterilisation on physico-chemical properties of antibacterial covalently cross-linked ε-polylysine/hyaluronic acid hydrogels, Carbohydr. Polym. 6 (2023) 100363, https://doi.org/10.1016/j.carpta.2023.100363.

[27] X. Bai, M. Gao, S. Syed, J. Zhuang, X. Xu, X.Q. Zhang, Bioactive hydrogels for bone regeneration, Bioact. Mater. 3 (2018) 401–417, https://doi.org/10.1016/j.bioactmat.2018.05.006.

[28] Y.Y. Chun, J.K. Wang, N.S. Tan, P.P. Chan, T.T. Tan, C. Choong, A periosteum-inspired 3D hydrogel-bioceramic composite for enhanced bone regeneration, Macromol. Biosci. 16 (2016) 276–287, https://doi.org/10.1002/mabi.201500258.

[29] J. Jeong, J.H. Kim, J.H. Shim, N.S. Hwang, C.Y. Heo, Bioactive calcium phosphate materials and applications in bone regeneration, Biomat. Res. 23 (2019) 1839–1851, https://doi.org/10.1186/s40824-018-0149-3.

[30] K. Wang, W. Cheng, Z. Ding, G. Xu, X. Zheng, M. Li, G. Lu, Q. Lu, Injectable silk/hydroxyapatite nanocomposite hydrogels with vascularization capacity for bone regeneration, J. Mater. Sci. Technol. 63 (2021) 172–181, https://doi.org/10.1016/j.jmst.2020.02.030.

[31] Z. Zou, L. Wang, Z. Zhou, Q. Sun, D. Liu, Y. Chen, H. Hu, Y. Cai, S. Lin, Z. Yu, B. Tan, W. Guo, Z. Ling, X. Zou, Simultaneous incorporation of PTH(1-34) and nano-hydroxyapatite into chitosan/alginate hydrogels for efficient bone regeneration, Bioact. Mater. 6 (2021) 1839–1851, https://doi.org/10.1016/j.bioactmat.2020.11.021.

[32] Y. Pan, Y. Zhao, R. Kuang, H. Liu, D. Sun, T. Mao, K. Jiang, X. Yang, N. Watanabe, K.H. Mayo, Q. Lin, J. Li, Injectable hydrogel-loaded nano-hydroxyapatite that improves bone regeneration and alveolar ridge promotion, Mater. Sci. Eng. C 116 (2020) 111158, https://doi.org/10.1016/j.msec.2020.111158.

[33] O. Faruq, B. Kim, A.R. Padalhin, G.H. Lee, B.T. Lee, A hybrid composite system of biphasic calcium phosphate granules loaded with hyaluronic acid-gelatin hydrogel for bone regeneration, J. Biomater. Appl. 32 (2017) 433–445, https://doi.org/10.1177/0885328217730688.

[34] J.A. Burdick, K.S. Anseth, Photoencapsulation of osteoblasts in injectable RGD-modified PEG hydrogels for bone tissue engineering, Biomaterials 23 (2002) 4315–4323, https://doi.org/10.1016/S0142-9612(02)00176-X.

[35] M. Fosca, A. Streza, I.V. Antoniac, G. Vadalà, J.V. Rau, Ion-doped calcium phosphate-based coatings with antibacterial properties, J. Funct. Biomater. 14 (2023) 250, https://doi.org/10.3390/jfb14050250.

[36] R. Zhao, S. Chen, W. Zhao, L. Yang, B. Yuan, V.S. Ioan, A.V. Iulian, X. Yang, X. Zhu, X.A. Zhang, A bioceramic scaffold composed of strontium-doped three-dimensional hydroxyapatite whiskers for enhanced bone regeneration in osteoporotic defects, Theranostics 10 (2020) 1572–1589, https://doi.org/10.7150/thno.40103.

[37] X. Ding, X. Li, C. L, M. Qi, Z. Zhang, X. Sun, L. Wang, Y. Zhou, Chitosan/dextran hydrogel constructs containing strontium-doped hydroxyapatite with enhanced osteogenic potential in rat cranium, ACS Biomater Sci. Eng. 5 (2019) 4574–4586, https://doi.org/10.1021/acsbiomaterials.9b00584.

[38] J. Wang, X. Wang, Z. Liang, W. Lan, Y. Wei, Y. Hu, L. Wang, Q. Lei, D. Huang, Injectable antibacterial Ag-HA/GelMA hydrogel for bone tissue engineering, Front. Bioeng. Biotechnol. 11 (2023) 1219460, https://doi.org/10.3389/fbioe.2023.1219460.

[39] Y. Shin, K.-H. Cheon, E.-H. Song, Y.-J. Seong, J.-U. Park, H.-E. Kim, S.-H. Jeong, Fluorine-ion-releasing injectable alginate nanocomposite hydrogel for enhanced bioactivity and antibacterial property, Int. J. Biol. Macromol. 123 (2019) 866–877, https://doi.org/10.1016/j.ijbiomac.2018.11.108.

[40] T.E.L. Douglas, M. Dziadek, S. Gorodzha, J. Liskova, G. Brackman, V. Vanhoorne, C. Vervaet, L. Balcaen, M. del Rosario Florez, A.R. Garcia, V. Boccaccini, T. Weinhardt, F. Baumbach, T. Vanhaecke, L. Coenye, M.A. Bacakova, R. A. Surmeneva, K. Surmenev, A.G. Skirtach Cholewa-Kowalska, Novel injectable gellan gum hydrogel composites incorporating Zn- and Sr-enriched bioactive glass microparticles: high-resolution X-ray microcomputed tomography, antibacterial and *in vitro* testing, J. Tissue Eng. Regen. Med. 12 (2018) 1313–1326, https://doi.org/10.1002/term.2654.

[41] L. Stipniece, A. Ramata-Stunda, J. Vecstaudza, I. Kreicberga, D. Livkisa, A. Rubina, A. Sceglovs, K. Salma-Ancane, A comparative study on physicochemical properties and *in vitro* biocompatibility of Sr-substituted and Sr ranelate-loaded hydroxyapatite nanoparticles, ACS Appl. Bio Mater. 6 (2023) 5264–5281, https://doi.org/10.1021/acsabm.3c00539.

[42] T.E. Robinson, E.A.B. Hughes, N.M. Eisenstein, L.M. Grover, S.C. Cox, The quantification of injectability by mechanical testing, J. Vis. Exp. 159 (2020) e61417, https://doi.org/10.3791/61417.

[43] T.T. Chen, Quantifying polymer crosslinking density using rheology and DMA. https://www.tainstruments.com/applications-notes/quantifying-polymer-crosslinking-density-using-rheology-and-dma/ (Accessed 16th August, 2024).

[44] J.M. Alonso, J. Andrade Del Olmo, R. Perez Gonzalez, V. Saez-Martinez, Injectable hydrogels: from laboratory to industrialization, Polymers (Basel) 13 (2021) 650, https://doi.org/10.3390/polym13040650.

[45] T. Levingstone, B. Ali, C. Kearney, N. Dunne, Hydroxyapatite sonosensitization of ultrasound-triggered, thermally responsive hydrogels: an on-demand delivery system for bone repair applications, J. Biomed. Mater. Res. 109 (2021) 1622–1633, https://doi.org/10.1002/jbm.b.34820.
[46] P. Bertsch, M. Diba, D.J. Mooney, S.C.G. Leeuwenburgh, Self-healing injectable hydrogels for tissue regeneration, Chem. Rev. 123 (2023) 834–873, https://doi.org/10.1021/acs.chemrev.2c00179.
[47] E.F. Burguera, H.H. Xu, L. Sun, Injectable calcium phosphate cement: effects of powder-to-liquid ratio and needle size, J. Biomed. Mater. Res. B Appl. Biomater. 84 (2008) 493–502, https://doi.org/10.1002/jbm.b.30896.
[48] S. Jacquart, S. Girod-Fullana, F. Brouillet, C. Pigasse, R. Siadous, M. Fatnassi, J. Grimoud, C. Rey, C. Roques, C. Combes, Injectable bone cement containing carboxymethyl cellulose microparticles as a silver delivery system able to reduce implant-associated infection risk, Acta Biomater. 145 (2022) 342–357, https://doi.org/10.1016/j.actbio.2022.04.015.
[49] M. Haghighi, K. Rezaei, General analytical schemes for the characterization of pectin-based edible gelled systems, ScientificWorldJournal 2012 (2012) 967407, https://doi.org/10.1100/2012/967407.
[50] A. Prince, Development of In Situ Forming Hydrogels for Intra-Articular Drug Delivery, Doctoral dissertation,, The University of Western Ontario, Canada, 2019, https://ir.lib.uwo.ca/etd/6077.
[51] K. Bouiahya, A. Oulguidoum, A. Laghzizil, M. Shalabi, J.M.M. Nunzi, S. Masse, Hydrophobic chemical surface functionalization of hydroxyapatite nanoparticles for naphthalene removal, Colloids Surf. A Physicochem. Eng. Asp. 595 (2020) 124706, https://doi.org/10.1016/j.colsurfa.2020.124706.
[52] X. Ran, X. Yu, J. He, Z. Xiao, Molecular mechanism of nano-hydroxyapatite surface changes from hydrophilic to hydrophobic, Asian J. Chem. 26 (2014) 5355–5359, https://doi.org/10.14233/ajchem.2014.18110.
[53] G. Kaya, F. Oytun, Rheological properties of injectable hyaluronic acid hydrogels for soft tissue engineering applications, Biointerface Res. Appl. Chem. 11 (2020) 8424–8430, https://doi.org/10.33263/BRIAC111.84248430.
[54] Y. Zhao, Z. Cui, B. Liu, J. Xiang, D. Qiu, Y. Tian, X. Qu, Z. Yang, An injectable strong hydrogel for bone reconstruction, Adv. Healthc. Mater. 8 (2019) 1900709, https://doi.org/10.1002/adhm.201900709.
[55] H. Zhou, C. Liang, Z. Wei, Y. Bai, S.B. Bhaduri, T.J. Webster, L. Bian, L. Yang, Injectable biomaterials for translational medicine, Mater. Today 28 (2019) 81–97, https://doi.org/10.1016/j.mattod.2019.04.020.
[56] G. Stojkov, Z. Niyazov, F. Picchioni, R.K. Bose, Relationship between structure and rheology of hydrogels for various applications, Gels 7 (2021) 255, https://doi.org/10.3390/gels7040255.
[57] B.M. Hong, G.L. Hong, M.A. Gwak, K.H. Kim, J.E. Jeong, J.Y. Jung, S.A. Park, W. H. Park, Self-crosslinkable hyaluronate-based hydrogels as a soft tissue filler, Int. J. Biol. Macromol. 185 (2021) 98–110, https://doi.org/10.1016/j.ijbiomac.2021.06.047.
[58] E. López-Ruiz, G. Jiménez, L. Álvarez de Cienfuegos, C. Antic, R. Sabata, J. A. Marchal, P. Gálvez-Martín, Advances of hyaluronic acid in stem cell therapy and tissue engineering, including current clinical trials, Eur. Cell. Mater. 37 (2019) 186–213, https://doi.org/10.22203/ecm.v037a12.
[59] K. Flegeau, O. Gauthier, G. Rethore, F. Autrusseau, A. Schaefer, J. Lesoeur, J. Veziers, A. Bresin, H. Gaitier, P. Weiss, Injectable silanized hyaluronic acid hydrogel/biphasic calcium phosphate granule composites with improved handling and biodegradability promote bone regeneration in rabbits, Biomater. Sci. 9 (2021) 5640–5651, https://doi.org/10.1039/D1BM00403D.
[60] H. Bakhtiari, A. Nouri, M. Khakbiz, M. Tolouei-Rad, Fatigue behaviour of load-bearing polymeric bone scaffolds: a review, Acta Biomater. 172 (2023) 16–37, https://doi.org/10.1016/j.actbio.2023.09.048.
[61] M.H. Chen, L.L. Wang, J.J. Chung, Y.H. Kim, P. Atluri, J.A. Burdick, Methods to assess shear-thinning hydrogels for application as injectable biomaterials, ACS Biomater Sci. Eng. 3 (2017) 3146–3160, https://doi.org/10.1021/acsbiomaterials.7b00734.
[62] S. Bashir, M. Hina, J. Iqbal, A.H. Rajpar, M.A. Mujtaba, N.A. Alghamdi, S. Wageh, K. Ramesh, S. Ramesh, Fundamental concepts of hydrogels: synthesis, properties, and their applications, Polymers (Basel) 12 (2020) 2702, https://doi.org/10.3390/polym12112702.
[63] K. Farbod, M.R. Nejadnik, J.A. Jansen, S.C.G. Leeuwenburgh, Interactions between inorganic and organic phases in bone tissue as a source of inspiration for design of novel nanocomposites, Tissue Eng. Part B Rev. 20 (2014) 173–188, https://doi.org/10.1089/ten.teb.2013.0221.
[64] M. Baniasadi, M. Minary-Jolandan, Alginate-collagen fibril composite hydrogel, Materials 8 (2) (2015) 799–814, https://doi.org/10.3390/ma8020799.
[65] L. Liu, P.H. Cooke, D.R. Coffin, M.L. Fishman, K.B. Hicks, Pectin and polyacrylamide composite hydrogels: effect of pectin on structural and dynamic mechanical properties, J. Appl. Polym. Sci. 92 (2004) 1893–1901, https://doi.org/10.1002/app.20174.
[66] R. Kocen, M. Gasik, A. Gantar, S. Novak, Viscoelastic behaviour of hydrogel-based composites for tissue engineering under mechanical load, Biomed. Mater. 12 (2) (2017) 025004, https://doi.org/10.1088/1748-605X/aa5b00.
[67] B.Y.S. Kumar, A.M. Isloor, G.C.M. Kumar, A.A.M. Inamuddin, Nanohydroxyapatite reinforced chitosan composite hydrogel with tunable mechanical and biological properties for cartilage regeneration, Sci. Rep. 9 (2019) 15957, https://doi.org/10.1038/s41598-019-52042-7.
[68] J.A. Sanchez-Fernandez, G. Presbitero-Espinosa, L. Pena-Paras, E.I.R. Pizana, K.P. V. Galvan, M. Vopalensky, I. Kumpova, L.E. Elizalde-Herrera, Characterization of sodium alginate hydrogels reinforced with nanoparticles of hydroxyapatite for biomedical applications, Polymers 13 (2021) 2927, https://doi.org/10.3390/polym13172927.
[69] A. Svarca, A. Grava, A. Dubnika, A. Ramata-Stunda, R. Narnickis, K. Aunina, E. Rieksta, M. Boroduskis, I. Jurgelane, L. Locs, D. Loca, Calcium phosphate/hyaluronic acid composite hydrogels for local antiosteoporotic drug delivery, Front. Bioeng. Biotechnol. 10 (2022) 917765, https://doi.org/10.3389/fbioe.2022.917765.
[70] W.A. Laftah, S. Hashim, A.N. Ibrahim, Polymer hydrogels: a review, Polym. - Plast. Technol. Eng. 50 (2011) 1475–1486, https://doi.org/10.1080/03602559.2011.593082.
[71] W. Feng, Z. Wang, Tailoring the swelling-shrinkable behavior of hydrogels for biomedical applications, Adv. Sci. 10 (2023) 2303326, https://doi.org/10.1002/advs.202303326.
[72] R. Foudazi, R. Zowada, I. Manas-Zloczower, D.L. Feke, Porous hydrogels: present challenges and future opportunities, Langmuir 39 (2023) 2092–2111, https://doi.org/10.1021/acs.langmuir.2c02253.
[73] L. Wang, S. Dong, Y. Liu, Y. Ma, J. Zhang, Z. Yang, W. Jiang, Y. Yuan, Fabrication of injectable, porous hyaluronic acid hydrogel based on an in-situ bubble-forming hydrogel entrapment process, Polymers (Basel) 12 (2020) 1138, https://doi.org/10.3390/polym12051138.
[74] J. Karvinen, M. Kellomaki, Characterization of self-healing hydrogels for biomedical applications, Eur. Polym. J. 181 (2022) 111641, https://doi.org/10.1016/j.eurpolymj.2022.111641.
[75] Z. Kaberova, E. Karpushkin, M. Nevoralová, M. Vetrík, M. Šlouf, M. Dušková-Smrčková, Microscopic structure of swollen hydrogels by scanning electron and light microscopies: artifacts and reality, Polymers 12 (2020) 578, https://doi.org/10.3390/polym12030578.
[76] A. Borzacchiello, L. Russo, B.M. Malle, K. Schwach-Abdellaoui, L. Ambrosio, Hyaluronic acid based hydrogels for regenerative medicine applications, Biomed. Res. Int. 2015 (2015) 242378, https://doi.org/10.1155/2015/871218.
[77] H. He, E. Luedke, X. Zhang, B. Yu, A. Schmitt, B. McClarren, V. Grignol, W. E. Carson, L.J. Lee, A naonoporous cell-therapy device with controllable biodegradation for long-term drug release, J. Control. Release 165 (3) (2013) 226–233, https://doi.org/10.1016/j.jconrel.2012.11.020.
[78] G.G. de Lima, L. Campos, A. Junqueira, D.M. Devine, M.J.D. Nugent, A novel pH-sensitive ceramic-hydrogel for biomedical applications, Polym. Adv. Technol. 26 (2015) 1439–1446, https://doi.org/10.1002/pat.3593.
[79] Y. Zhu, H. Jiang, S.H. Ye, T. Yoshizumi, W.R. Wagner, Tailoring the degradation rates of thermally responsive hydrogels designed for soft tissue injection by varying the autocatalytic potential, Biomaterials 53 (2015) 484–493, https://doi.org/10.1016/j.biomaterials.2015.02.100.
[80] S. Utech, A.R. Boccaccini, A review of hydrogel-based composites for biomedical applications: enhancement of hydrogel properties by addition of rigid inorganic fillers, J. Mater. Sci. 51 (2016) 271–310, https://doi.org/10.1007/s10853-015-9382-5.
[81] S. Wei, J.X. Ma, L. Xu, Biodegradable materials for bone defect repair, Military Med. Res. 7 (2020) 54, https://doi.org/10.1186/s40779-020-00280-6.
[82] X. Sheng, C. Li, Z. Wang, Y. Xu, Y. Sun, W. Zhang, H. Liu, J. Wang, Advanced applications of strontium-containing biomaterials in bone tissue engineering, Mater. Today Bio. 20 (2023), https://doi.org/10.1016/j.mtbio.2023.100636.
[83] L.C. Chow, L. Sun, B. Hockey, Properties of nanostructured hydroxyapatite prepared by a spray drying technique, J. Res. Natl. Inst. Stand. Technol. 109 (2004) 543–551, doi:10.6028%2Fjres.109.041.
[84] H. Xie, Z. Gu, Y. He, J. Xu, C. Xu, L. Li, Q. Ye, Microenvironment construction of strontium–calcium-based biomaterials for bone tissue regeneration: the equilibrium effect of calcium to strontium, J. Mater. Chem. B 6 (2018) 2332–2339, https://doi.org/10.1039/C8TB00306H.
[85] T.J. Silhavy, D. Kahne, S. Walker, The bacterial cell envelope, Cold Spring Harb. Perspect. Biol. 2 (5) (2010) a000414, https://doi.org/10.1101/cshperspect.a000414.
[86] V. Murugesan, M. Vaiyapuri, A. Murugeasan, Fabrication and characterization of strontium substituted chitosan modify hydroxyapatite for biomedical applications, Inorg. Chem. Comm. 142 (2022) 109653, https://doi.org/10.1016/j.inoche.2022.109653.
[87] E. Filova, T. Suchy, Z. Sucharda, M. Supova, M. Zaloudkova, K. Balik, V. Lisa, M. Slouf, L. Bacakova, Support for the initial attachment, growth and differentiation of MG-63 cells: a comparison between nano-size hydroxyapatite and micro-size hydroxyapatite in composites, Int. J. Nanomedicine 9 (2014) 3687–3706, https://doi.org/10.2147/IJN.S56661.
[88] S.-W. Tsai, Y.-W. Hsu, W.-L. Pan, F.-Y. Hsu, The effect of strontium-substituted hydroxyapatite nanofibrous matrix on osteoblast proliferation and differentiation, Membranes 11 (2021) 624, https://doi.org/10.3390/membranes11080624.
[89] Y. Hao, H. Yan, X. Wang, B. Zhu, C. Ning, S. Ge, Evaluation of osteoinduction and proliferation on nano-Sr-HAP: a novel orthopedic biomaterial for bone tissue regeneration, J. Nanosci. Nanotechnol. 12 (2012) 207–212, https://doi.org/10.1166/jnn.2012.5125.
[90] S. Maeno, Y. Niki, H. Matsumoto, H. Morioka, T. Yatabe, A. Funayama, Y. Toyama, T. Taguchi, J. Tanaka, The effect of calcium ion concentration on osteoblast viability, proliferation and differentiation in monolayer and 3D culture, Biomaterials 26 (2005) 4847–4855, https://doi.org/10.1016/j.biomaterials.2005.01.006.
[91] L. Gritsch, M. Maqbool, V. Mourino, F.E. Ciraldo, M. Cresswell, P.R. Jackson, C. Lovell, A.R. Boccaccini, Chitosan/hydroxyapatite composite bone tissue engineering scaffolds with dual and decoupled therapeutic ion delivery: copper and strontium, J. Mater. Chem. B 7 (2019) 6109–6124, https://doi.org/10.1039/C9TB00897G.

[92] J. Liu, S.C.F. Rawlinson, R.G. Hill, F. Fortune, Strontium-substituted bioactive glasses in vitro osteogenic and antibacterial effects, Dent. Mater. 32 (2016) 412–422, https://doi.org/10.1016/j.dental.2015.12.013.
[93] Y. Cheng, L. Huang, Y. Wang, Q. Huo, Y. Shao, H. Bao, Z. Li, Y. Liu, X. Li, Strontium promotes osteogenic differentiation by activating autophagy via the AMPK/mTOR signaling pathway in MC3T3-E1 cells, Int. J. Mol. Med. 44 (2019) 652–660, https://doi.org/10.3892/ijmm.2019.4216.
[94] F. Boukhechba, T. Balaguer, J.-F. Michiels, K. Ackermann, D. Quincey, J.-M. Bouler, W. Pyerin, G.F. Carle, N. Rochet, Human primary osteocyte differentiation in a 3D culture system, J. Bone Miner. Res. 24 (2009) 1927–1935, https://doi.org/10.1359/jbmr.090517.
[95] G. Nasello, P. Alaman-Diez, J. Schiavi, M.A. Perez, L. McNamara, J.M. Garcia-Aznar, Primary human osteoblasts cultured in a 3D microenvironment create a unique representative model of their differentiation into osteocytes, Front. Bioeng. Biotechnol. 8 (2020) 336, https://doi.org/10.3389/fbioe.2020.00336.
[96] M. Izumiya, M. Haniu, K. Ueda, H. Ishida, C. Ma, H. Ideta, A. Sobajima, K. Ueshiba, T. Uemura, N. Saito, H. Haniu, Evaluation of MC3T3-E1 cell osteogenesis in different cell culture media, Int. J. Mol. Sci. 22 (2021) 7752, https://doi.org/10.3390/ijms22147752.
[97] Y. Zhuang, A. Liu, S. Jiang, U. Liaqat, K. Lin, W. Sun, C. Yuan, Promoting vascularized bone regeneration via strontium-incorporated hydroxyapatite bioceramic, Mater. Des. 234 (2023) 112313, https://doi.org/10.1016/j.matdes.2023.112313.
[98] D. Marx, A.R. Yazdi, M. Papini, M. Towler, A review of the latest insights into the mechanism of action of strontium in bone, Bone Rep. 12 (2020) 100273, https://doi.org/10.1016/j.bonr.2020.100273.
[99] H.W. Kim, Y.J. Kim, Fabrication of strontium-substituted hydroxyapatite scaffolds using 3D printing for enhanced bone regeneration, J. Mater. Sci. 56 (2021) 1673–1684, https://doi.org/10.1007/s10853-020-05391-y.
[100] X. Lin, S. Patil, Y.-G. Gao, A. Qian, The bone extracellular matrix in bone formation and regeneration, Front. Pharmacol. 11 (2020) 757, https://doi.org/10.3389/fphar.2020.00757.
[101] R. Fattahi, F. Mohebichamkhorami, N. Taghipour, S.H. Keshel, The effect of extracellular matrix remodeling on material-based strategies for bone regeneration: review article, Tissue Cell 76 (2022) 101748, https://doi.org/10.1016/j.tice.2022.101748.
[102] L. Liang, D.-P. Zhu, S.-S. Guo, D. Zhang, T. Zhang, MMP-1 gene polymorphism in osteoporosis, Eur. Rev. Med. Pharmacol. Sci. 23 (2019) 67–72, https://doi.org/10.26355/eurrev_201908_18631.
[103] R.J. Wenstrup, J.L. Fowlkes, D.P. Witte, J.B. Florer, Discordant expression of osteoblast markers in MC3T3-E1 cells that synthesize a high turnover matrix, J. Biol. Chem. 271 (1996) 10271–10276, https://doi.org/10.1074/jbc.271.17.10271.